J. Fluid Mech. (2010), *vol.* 665, *pp.* 418–456.
doi:10.1017/S0022112010004003

Film flow over heated wavy inclined surfaces

S. J. D. D'ALESSIO[1]†, J. P. PASCAL[2], H. A. JASMINE[2] AND K. A. OGDEN[1]

[1]Department of Applied Mathematics, University of Waterloo, Waterloo, Ontario, Canada N2L 3G1
[2]Department of Mathematics, Ryerson University, Toronto, Ontario, Canada M5B 2K3

(Received 9 August 2009; revised 25 July 2010; accepted 26 July 2010;
first published online 27 October 2010)

The two-dimensional problem of gravity-driven laminar flow of a thin layer of fluid down a heated wavy inclined surface is discussed. The coupled effect of bottom topography, variable surface tension and heating has been investigated both analytically and numerically. A stability analysis is conducted while nonlinear simulations are used to validate the stability predictions and also to study thermocapillary effects. The governing equations are based on the Navier–Stokes equations for a thin fluid layer with the cross-stream dependence eliminated by means of a weighted residual technique. Comparisons with experimental data and direct numerical simulations have been carried out and the agreement is good. New interesting results regarding the combined role of surface tension and sinusoidal topography on the stability of the flow are presented. The influence of heating and the Marangoni effect are also deduced.

Key words: instability, Marangoni convection, thermocapillarity

1. Introduction

A shallow layer of fluid resting on a heated horizontal surface is known to become unstable to both buoyancy-driven convection and thermocapillary convection. If the fluid layer is sufficiently thin thermocapillary convection, induced by gradients in surface tension, is expected to be the dominant instability mechanism. This is known as the Marangoni effect. It has even been suggested (Smith 1966) that the instability observed by Bénard (1900) was likely due to the Marangoni effect rather than the buoyancy effects. When the fluid layer is allowed to flow over an inclined heated surface the dynamics are controlled by several competing mechanisms. As noted by Ruyer-Quil *et al.* (2005), first there is the classical long-wave instability resulting from isothermal flows, which was originally studied experimentally by Kapitza & Kapitza (1949). The linear stability properties associated with this mode are now well known due to the work by Benjamin (1957) and Yih (1963) and the key finding is that the critical Reynolds number, Re_{crit}, beyond which the flow becomes unstable, is given by $Re_{crit} = 5\cot\beta/6$, where β is the angle of inclination. This result has been verified by the experiments of Liu, Paul & Gollub (1993) and a physical mechanism

† Email address for correspondence: sdalessio@uwaterloo.ca

for this long-wave instability was provided by Smith (1990). In addition, Goussis & Kelly (1991) have identified two other instability modes, which result from the Marangoni instability brought on by an inhomogeneous temperature field: a short-wave instability (Pearson 1958) and a long-wave instability (Scriven & Sternling 1964; Smith 1966).

The problem of thin-film flow over an even inclined heated surface was studied by Kalliadasis, Kiyashko & Demekhin (2003*b*) and Kalliadasis *et al.* (2003*a*), and later revisited by Ruyer-Quil *et al.* (2005), Scheid *et al.* (2005*a*) and Trevelyan *et al.* (2007). In these studies the focus was on the long-wave instability. A method to study the long-wave nature of the instability was devised by Benney (1966). This method involves introducing a small long-wave parameter and carrying out an expansion in this parameter, which ultimately leads to a single evolution equation, commonly referred to as the Benney equation, for the free surface. This procedure, along with similar approaches, has proved to be very successful in determining the threshold of instability and has been thoroughly reviewed by Chang (1994). The evolutionary equations for the free surface emerging from these techniques have been applied to numerous problems ranging from Newtonian to non-Newtonian fluids (Lin 1974; Nepomnyashchy 1974; Oron, Davis & Bankoff 1997; Usha & Uma 2004), isothermal to non-isothermal flows (Lin 1975; Scheid *et al.* 2005*a*; Joo, Davis & Bankoff 1991; Mukhopadhyay & Mukhopadhyay 2007; Samanta 2008), impermeable to porous surfaces (Thiele, Goyeau & Velarde 2009), even to uneven bottom topography (Tougou 1978; Davalos-Orozco 2007) and also combinations thereof (Usha & Uma 2004; Khayat & Kim 2006; Thiele *et al.* 2009), to list a few. In addition, an extensive review of the dynamics and stability of thin-film flows has recently been prepared by Craster & Matar (2009). One serious drawback of the Benney equation lies in the fact that the solution becomes singular (i.e. it blows up) in finite time shortly after criticality. Since solutions to the full Navier–Stokes equations do not display such a behaviour, the singularity present in the Benney equation, as pointed out by Rosenau, Oron & Hyman (1992), Salamon, Armstrong & Brown (1994), Oron & Gottlieb (2004) and Scheid *et al.* (2005*b*), bears no physical relevance.

Situations involving falling films occur often in environmental and industrial settings and continue to interest researchers. Because of this, considerable effort has been invested in modelling such flows. One class of models is known as integral-boundary-layer (IBL) models. The basic idea behind these models is first to simplify the governing Navier–Stokes equations by formulating them in terms of a shallowness parameter and neglecting terms that are deemed to be small. Next, the cross-stream dependence is eliminated by depth-integrating the equations and prescribing the velocity variation with respect to depth. The standard choice is the parabolic velocity profile, which follows from the laminar steady balance between gravity and viscosity. The original IBL model was developed by Shkadov (1967) and it was first-order since only terms that are $O(\delta)$ were retained in the equations, where δ is the shallowness parameter. The IBL approach has been shown to accurately describe the flow in the non-uniform and transient regime and also to capture the flow under supercritical conditions (Alekseenko, Nakoryakov & Pokusaev 1985; Julien & Hartley 1986). Despite the success and attempts to improve them (Prokopiou, Cheng & Chang 1991), IBL models are plagued with the serious flaw that they are unable to reproduce the critical conditions for the onset of instability as predicted by Orr–Sommerfeld calculations and experiments (Kapitza & Kapitza 1949; Benjamin 1957; Yih 1963; Liu *et al.* 1993).

The deficiency exhibited by IBL models has been remedied by Ruyer-Quil & Manneville (2000, 2002) using a weighted residual technique. The second-order equations emerging from this method can be expressed as a system of two equations governing the fluid depth, h, and the flow rate, q, and can be regarded as the modified IBL equations. The modified IBL model not only correctly predicts the threshold for the onset of linear instability, but also provides an accurate description of the nonlinear development of waves up to relatively high Reynolds numbers when compared with the experimental observations of Liu, Schneider & Gollub (1995) and the direct numerical simulations of Ramaswamy, Chippada & Joo (1996). The ability of this model to accurately describe unstable flows far from criticality qualifies it as a major improvement over the Benney equation which is only valid near criticality. The weighted residual method appears to be gaining popularity as it has been successfully applied to other problems. For example, Ruyer-Quil *et al.* (2005) and Scheid *et al.* (2005*a*) have used it to study thermocapillary effects for the problem of film flow over an even inclined heated surface; Oron & Heining (2008) implemented it to investigate film flow falling down a corrugated vertical wall; and recently, D'Alessio, Pascal & Jasmine (2009) have generalized the method to model the flow down an uneven incline, to name a few.

The main purpose of the present investigation is to extend the thermocapillary studies of Kalliadasis *et al.* (2003*a*, *b*), Ruyer-Quil *et al.* (2005), Scheid *et al.* (2005*a*) and Trevelyan *et al.* (2007) by accounting for bottom topography and hence widen the range of applications. Both numerical and analytical methods have been utilized to better understand how the complicated interplay between heating, strong surface tension and bottom topography affect the stability of the flow. The underlying assumptions made here are that the flow remains laminar and two-dimensional for all time, t. These conditions are expected to be satisfied if Re and $\cot\beta$ are $O(1)$. Although the governing equations will be derived for arbitrary bottom topography, we will focus our investigation on wavy inclines characterized by an amplitude and a wavelength. While the isothermal counterpart of this problem has been reported in various numerical, analytical and experimental studies (Trifonov 1998, 2007*a*, *b*; Vlachogiannis & Bontozoglou 2002; Wierschem & Aksel 2003; Balmforth & Mandre 2004; Wierschem, Lepski & Aksel 2005; Davalos-Orozco 2008; Häcker & Uecker 2009; Heining & Aksel 2009; Heining *et al.* 2009), this study represents the first work to tackle the non-isothermal case.

The paper is structured as follows. In § 2, we derive a mathematical model to describe the problem of laminar flow over a heated inclined surface having arbitrary bottom topography. The equations are expressed in terms of the fluid depth (h), flow rate (q) and surface temperature (θ) using a second-order weighted residual approach. As pointed out by D'Alessio *et al.* (2009), significant changes between first-order and second-order models can result. This is expected to be the case for non-isothermal flows as well and thus motivates the need to resort to a second-order model. Then, in § 3, a stability analysis is conducted for the case of sinusoidal bottom topography. Following this, nonlinear numerical simulations along with comparisons with existing data and direct numerical simulations are presented in § 4. These results serve to validate the mathematical model as well as the analytical predictions, and also to study thermocapillary effects. Lastly, the key points are summarized in the concluding section. Three appendices are also included. Appendix A is devoted to deriving the Benney equation corresponding to our problem. Appendix B lists various coefficients appearing in the stability analysis in § 3 and Appendix C outlines the numerical solution procedure used to obtain the results in § 4.

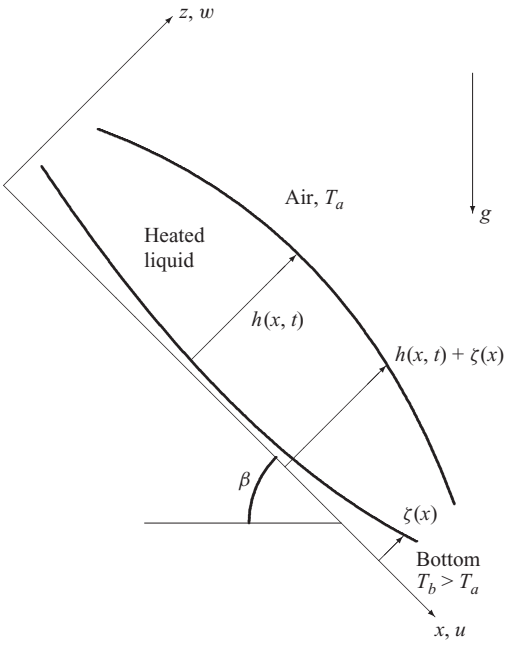

FIGURE 1. The flow configuration.

2. Governing equations

We consider the two-dimensional laminar flow of a thin layer of a Newtonian fluid along an uneven heated inclined surface, which is maintained at constant temperature T_b as shown in figure 1. The adopted (x, z) coordinate system is oriented so that the x-axis points along the incline, in the downhill direction, at an angle of β with the horizontal, while the z-axis points in the upward normal direction. The bottom is taken to be periodic having the form

$$z = \zeta(x) = A_b \cos\left(\frac{2\pi x}{\lambda_b}\right), \tag{2.1}$$

where A_b denotes the amplitude of the undulations and λ_b denotes the corresponding wavelength. The fluid velocity is denoted by $\boldsymbol{u} = (u, w)^{\mathrm{T}}$.

We scale the equations as follows. For the vertical length scale, we choose the Nusselt thickness, H, resulting from a flow rate, Q, which is given by

$$H = \left(\frac{3\mu Q}{\rho g \sin\beta}\right)^{1/3}, \tag{2.2}$$

where g is the acceleration due to gravity, and ρ and μ are the fluid density and viscosity, respectively. The pressure is scaled using ρU^2, where $U = Q/H$ is the velocity scale. The corresponding time scale is taken to be l/U, where l is the horizontal length scale which is taken to be λ_b. Lastly, the temperature is scaled according to $\Delta T = T_b - T_a$, where T_a is the constant ambient air temperature and $T_b > T_a$.

While the fluid properties ρ, μ and the thermal diffusivity, κ, are assumed to remain constant, the surface tension, σ, is allowed to vary with temperature, T, in the usual fashion,

$$\sigma(T) = \sigma_0 - \gamma(T - T_a), \tag{2.3}$$

where γ is a positive constant for most common fluids. Here, we have assumed that the fluid layer is sufficiently thin so that buoyancy effects will be negligible. In addition, it is assumed that the liquid is non-volatile so that evaporation can be ignored.

The governing two-dimensional Navier–Stokes and energy equations can then be rendered in the following dimensionless form:

$$\frac{\partial u}{\partial x} + \frac{\partial w}{\partial z} = 0, \tag{2.4}$$

$$\delta Re \frac{\mathrm{D}u}{\mathrm{D}t} = -\delta Re \frac{\partial p}{\partial x} + 3 + \delta^2 \frac{\partial^2 u}{\partial x^2} + \frac{\partial^2 u}{\partial z^2}, \tag{2.5}$$

$$\delta^2 Re \frac{\mathrm{D}w}{\mathrm{D}t} = -Re \frac{\partial p}{\partial z} - 3\cot\beta + \delta^3 \frac{\partial^2 w}{\partial x^2} + \delta \frac{\partial^2 w}{\partial z^2}, \tag{2.6}$$

$$\delta Re Pr \frac{\mathrm{D}T}{\mathrm{D}t} = \delta^2 \frac{\partial^2 T}{\partial x^2} + \frac{\partial^2 T}{\partial z^2}, \tag{2.7}$$

where $\mathrm{D}/\mathrm{D}t$ denotes the two-dimensional material derivative, $\delta = H/l = H/\lambda_b$ is the shallowness parameter, $Re = UH/\nu$ is the Reynolds number, $Pr = \nu/\kappa$ is the Prandtl number and $\nu = \mu/\rho$ is the kinematic viscosity.

We next assume that Re and Pr are of order unity and discard terms that are of order δ^3 in (2.4)–(2.7). Based on the result $Re_{crit} = 5\cot\beta/6$ for isothermal flow over an even incline, we expect our assumption to be valid for sufficiently steep inclinations since for sufficiently gentle inclinations $\cot\beta$ will become of order $1/\delta$ and thus more terms in the equations will need to be retained. The equations then will be as follows:

$$\frac{\partial u}{\partial x} + \frac{\partial w}{\partial z} = 0, \tag{2.8}$$

$$\delta Re \frac{\mathrm{D}u}{\mathrm{D}t} = -\delta Re \frac{\partial p}{\partial x} + 3 + \delta^2 \frac{\partial^2 u}{\partial x^2} + \frac{\partial^2 u}{\partial z^2}, \tag{2.9}$$

$$\delta^2 Re \frac{\mathrm{D}w}{\mathrm{D}t} = -Re \frac{\partial p}{\partial z} - 3\cot\beta + \delta \frac{\partial^2 w}{\partial z^2}, \tag{2.10}$$

$$\delta Re Pr \frac{\mathrm{D}T}{\mathrm{D}t} = \delta^2 \frac{\partial^2 T}{\partial x^2} + \frac{\partial^2 T}{\partial z^2}. \tag{2.11}$$

The dynamic conditions at the free surface are (Nepomnyashchy, Velarde & Colinet 2002):

$$p = \frac{2}{ReF}\left(\delta^3 \left[\frac{\partial z_1}{\partial x}\right]^2 \frac{\partial u}{\partial x} + \delta \frac{\partial w}{\partial z} - \delta \frac{\partial z_1}{\partial x}\frac{\partial u}{\partial z} - \delta^3 \frac{\partial z_1}{\partial x}\frac{\partial w}{\partial x}\right) - \frac{\delta^2(We - MaT)}{F^{3/2}} \frac{\partial^2 z_1}{\partial x^2}, \tag{2.12}$$

$$-\delta Ma Re \sqrt{F}\left(\frac{\partial T}{\partial x} + \frac{\partial z_1}{\partial x}\frac{\partial T}{\partial z}\right) = G\left(\frac{\partial u}{\partial z} + \delta^2 \frac{\partial w}{\partial x}\right) - 4\delta^2 \frac{\partial z_1}{\partial x}\frac{\partial u}{\partial x}, \tag{2.13}$$

$$-Bi\sqrt{F}T = \frac{\partial T}{\partial z} - \delta^2 \frac{\partial z_1}{\partial x}\frac{\partial T}{\partial x}. \tag{2.14}$$

Here,

$$F = 1 + \delta^2 \left[\frac{\partial z_1}{\partial x}\right]^2 \quad \text{and} \quad G = 1 - \delta^2 \left[\frac{\partial z_1}{\partial x}\right]^2, \tag{2.15}$$

where $z_1 = \zeta(x) + h(x,t)$ denotes the free surface, $We = \sigma_0 H/(\rho Q^2)$ is the Weber number, $Ma = \gamma \Delta T/(\rho U^2 H)$ is the Marangoni number, $Bi = \alpha_g H/(\rho c_p \kappa)$ is the Biot number with α_g denoting the heat transfer coefficient across the liquid–air interface and c_p is the specific heat at constant pressure of the liquid. We note that these conditions are responsible for the coupling between the momentum and energy equations and that the surface-tension term is of second order or larger if the Weber number is of order $1/\delta$ or larger.

As before, to order δ^2 these conditions yield:

$$\left.\begin{aligned} & p - \frac{2\delta}{Re}\frac{\partial w}{\partial z} + \delta^2(We - MaT)\frac{\partial^2 z_1}{\partial x^2} = 0, \\ & \frac{\partial u}{\partial z} - 4\delta^2 \frac{\partial z_1}{\partial x}\frac{\partial u}{\partial x} + \delta^2 \frac{\partial w}{\partial x} + MaRe\delta\left(\frac{\partial T}{\partial x} + \frac{\partial z_1}{\partial x}\frac{\partial T}{\partial z}\right) = 0, \\ & -BiT\left(1 + \frac{\delta^2}{2}\left[\frac{\partial z_1}{\partial x}\right]^2\right) = \frac{\partial T}{\partial z} - \delta^2 \frac{\partial z_1}{\partial x}\frac{\partial T}{\partial x}, \end{aligned}\right\} \quad \text{at } z = z_1. \tag{2.16}$$

The kinematic condition dictating the position of the free surface is given by

$$w = \frac{\partial h}{\partial t} + u\frac{\partial h}{\partial x} + u\zeta'(x), \tag{2.17}$$

and the scaled bottom profile is

$$\zeta(x) = a_b \cos(2\pi x), \quad \text{where } a_b = \frac{A_b}{H} = \frac{1}{\delta}\frac{A_b}{\lambda_b}. \tag{2.18}$$

In this study, we will consider small bottom waviness having A_b/λ_b of order δ and thus a_b will be of order unity. At the interface between the fluid layer and the impermeable bottom, the tangential and normal fluid velocity components are zero. This results in the no-slip and impermeability conditions

$$u = w = 0 \quad \text{at } z = \zeta(x). \tag{2.19}$$

Finally, we have the bottom temperature condition

$$T = 1 \quad \text{at } z = \zeta(x). \tag{2.20}$$

For small aspect ratio flows, which are slowly varying in the x direction, a depth averaging of the equations is warranted. This removes the z-dependence from the problem and yields a one-dimensional problem, which is better suited for mathematical analyses. By depth-integrating the continuity equation (2.8) and incorporating the kinematic condition, one obtains

$$\frac{\partial h}{\partial t} + \frac{\partial q}{\partial x} = 0, \tag{2.21}$$

where the flow rate, q, is given by

$$q = \int_{\zeta(x)}^{\zeta(x)+h} u \, \mathrm{d}z. \tag{2.22}$$

Integrating (2.10) from $z = z_1 = h + \zeta$ to z and substituting the value for the pressure at the free surface from the first condition in (2.16) provides the following expression

for the total pressure:

$$p = \frac{3\cot\beta}{Re}(z_1 - z) - \frac{\delta}{Re}\frac{\partial u}{\partial x}\bigg|_{z=z_1} - \frac{\delta}{Re}\frac{\partial u}{\partial x} - \delta^2(We - MaT)\frac{\partial^2 z_1}{\partial x^2} - \delta^2\int_{z_1}^{z}\frac{Dw}{Dt}\,\mathrm{d}z. \quad (2.23)$$

This can be used to eliminate the pressure from the x-momentum equation (2.9). It follows that the inertia term in the above can be discarded owing to the factor of δ multiplying the pressure gradient is (2.9), which makes it of order δ^3 when Re is of order unity.

Next, we implement the weighted residual technique to eliminate the z-dependence. This procedure begins by assuming the following profiles for the velocity and temperature:

$$u = \frac{3q}{2h^3}b + \frac{\delta Ma\,Re}{4h}b_1\frac{\partial\theta}{\partial x}, \quad (2.24)$$

$$T = 1 + \frac{(\theta - 1)}{h}(z - \zeta), \quad (2.25)$$

where b and b_1 are given by

$$b = (z - \zeta)(2h - z + \zeta), \quad b_1 = (z - \zeta)(2h - 3z + 3\zeta), \quad (2.26)$$

and are to be viewed as basis functions with respect to the z-coordinate. Here, we have introduced the interfacial temperature $\theta(x, t) = T(x, z = z_1, t)$. We note that the above-assumed profile for u satisfies the no-slip condition $u = 0$ at $z = \zeta$ and the leading-order free-surface condition

$$\frac{\partial u}{\partial z} = -\delta Ma\,Re\frac{\partial\theta}{\partial x} \quad \text{at } z = z_1. \quad (2.27)$$

Although the profile for T satisfies the bottom condition $T = 1$ on $z = \zeta$, it does not satisfy the free-surface condition given by (2.16). In fact, it is impossible for the profile to satisfy both. However, as noted by Kalliadasis *et al.* (2003*a*), the free-surface condition is incorporated into the energy equation when it is integrated over the fluid thickness, as described below.

In accordance with the Galerkin approach, we take b as the weight function and multiply (2.9) by b and integrate with respect to z from $\zeta(x)$ to $h + \zeta(x)$. Likewise, for the energy equation we take the weight function to be $(z - \zeta)$ and multiply (2.11) by this and again integrate from $\zeta(x)$ to $h + \zeta(x)$. After some algebra, we obtain the following dimensionless equations for the flow variables h, q and θ:

$$\frac{\partial h}{\partial t} + \frac{\partial q}{\partial x} = 0, \quad (2.28)$$

$$\begin{aligned}\frac{\partial q}{\partial t} + \frac{\partial}{\partial x}\left[\frac{9}{7}\frac{q^2}{h} + \frac{5}{4}\frac{\cot\beta}{Re}h^2 + \frac{5}{4}Ma\theta\right] &= \frac{q}{7h}\frac{\partial q}{\partial x} + \frac{5}{2\delta Re}\left(h - \frac{q}{h^2}\right) + \frac{5}{6}\delta^2 Weh\left(\frac{\partial^3 h}{\partial x^3} + \zeta'''\right) - \frac{5\cot\beta}{2Re}\zeta' h + \frac{\delta}{Re} \\ &\times \left[\frac{9}{2}\frac{\partial^2 q}{\partial x^2} - \frac{9}{2h}\frac{\partial q}{\partial x}\frac{\partial h}{\partial x} + \frac{4q}{h^2}\left(\frac{\partial h}{\partial x}\right)^2 - \frac{6q}{h}\frac{\partial^2 h}{\partial x^2} - \frac{5\zeta' q}{2h^2}\frac{\partial h}{\partial x} - \frac{15\zeta'' q}{4h} - \frac{5(\zeta')^2 q}{h^2}\right] \\ &+ \frac{\delta ReMa}{16}\left[\frac{h^2}{3}\frac{\partial^2\theta}{\partial x\partial t} + \frac{15hq}{14}\frac{\partial^2\theta}{\partial x^2} + \frac{19h}{21}\frac{\partial q}{\partial x}\frac{\partial\theta}{\partial x} + \frac{5q}{7}\frac{\partial h}{\partial x}\frac{\partial\theta}{\partial x}\right], \end{aligned} \quad (2.29)$$

$$h\frac{\partial\theta}{\partial t}+\frac{27q}{20}\frac{\partial\theta}{\partial x}-\frac{7}{40}(1-\theta)\frac{\partial q}{\partial x}$$
$$=\frac{3}{\delta RePrh}[1-\theta(1+Bih)]+\frac{\delta}{RePr}\left[(1-\theta)\frac{\partial^2 h}{\partial x^2}+h\frac{\partial^2\theta}{\partial x^2}+\frac{\partial h}{\partial x}\frac{\partial\theta}{\partial x}\right.$$
$$-\left(\frac{3Bi\theta}{2}+\frac{2(1-\theta)}{h}\right)\left(\frac{\partial h}{\partial x}\right)^2-3\zeta'\left(\frac{(1-\theta)}{h}+Bi\theta\right)\frac{\partial h}{\partial x}+\frac{3\zeta''}{2}(1-\theta)$$
$$\left.-\frac{3Bi(\zeta')^2\theta}{2}\right]+\frac{3\delta ReMa}{80}\left[2h^2\left(\frac{\partial\theta}{\partial x}\right)^2-h^2(1-\theta)\frac{\partial^2\theta}{\partial x^2}-2h(1-\theta)\frac{\partial h}{\partial x}\frac{\partial\theta}{\partial x}\right]. \quad (2.30)$$

In the isothermal limit, the above system reduces to the second-order modified IBL equations of D'Alessio *et al.* (2009) for an uneven bottom, and further setting $\zeta\equiv 0$ recovers the second-order modified IBL equations of Ruyer-Quil & Manneville (2000) for an even bottom. In arriving at these equations, we have assumed that the parameters Re, Ma, Bi, Pr and $\cot\beta$ are all of order unity and that We is of order $1/\delta$ or larger.

3. Stability analysis

To examine how small disturbances will evolve when superimposed on a steady equilibrium flow, we begin by first exploring the even bottom case and linearize equations (2.28)–(2.30) using

$$h=1+\hat{h},\quad q=1+\hat{q},\quad \theta=\frac{1}{1+Bi}+\hat{\theta}. \quad (3.1)$$

Here, we have made use of the constant steady-state solutions $h_s=q_s=1$ and $\theta_s=1/(1+Bi)$. We note from (2.28) that the steady-state solution for q is a constant. Thus, we select the scale for the flow rate, Q, such that $q=q_s=1$ in dimensionless form. Next, we set

$$\hat{h}=h_0 e^{ikx}e^{\sigma t},\quad \hat{q}=q_0 e^{ikx}e^{\sigma t},\quad \hat{\theta}=\theta_0 e^{ikx}e^{\sigma t}, \quad (3.2)$$

and combine the three equations. In order to make analytical progress, we only retain terms up to order δ to arrive at the following:

$$\frac{15\delta BiMak^2}{4RePr(1+Bi)}=\frac{5\delta}{2Re}(\sigma+3ik)\left(\sigma+\frac{27}{20}ik\right)+\frac{3(1+Bi)}{RePr}\left[\delta\sigma\left(\sigma+\frac{17}{7}ik\right)\right.$$
$$\left.+\delta k^2\left(\frac{5\cot\beta}{2Re}-\frac{9}{7}\right)+\frac{5}{2Re}(\sigma+3ik)\right]. \quad (3.3)$$

If $\sigma=\sigma_r+i\sigma_i$, then for neutral stability $\sigma_r=0$. Substituting $\sigma=i\sigma_i$ into the above and separating into real and imaginary parts, one finds $\sigma_i=-3k$ resulting from the imaginary part which yields a dimensionless phase speed of $c=-\sigma_i/k=3$. When this is substituted into the real part, the following instability threshold emerges:

$$Re_{crit}^{even}=\frac{10(1+Bi)^2\cot\beta}{5MaBi+12(1+Bi)^2}. \quad (3.4)$$

We note that for arbitrary Ma the above expression recovers the isothermal result when $Bi=0$ or $Bi\to\infty$ (although it must be remembered that we have assumed that Bi is of order unity). Moreover, it reveals that the Marangoni effect destabilizes the flow since $Re_{crit}^{even}<5\cot\beta/6$ for $Ma>0$ (i.e. $T_b>T_a$). It can easily be shown that

Re_{crit}^{even} attains a minimum value of

$$Re_{crit,min}^{even} = \frac{40\cot\beta}{48+5Ma}, \tag{3.5}$$

when $Bi=1$. This destabilization of the flow was also obtained by Trevelyan *et al.* (2007) in their study of heated falling films using both specified heat flux and specified temperature bottom boundary conditions. It is interesting to point out that when there is no heat transfer across the liquid–air interface (i.e. $Bi=0$) the Marangoni effect has no influence on the stability of the flow. This is easily explained by referring to the steady-state temperature profile

$$T_s(z) = 1 - \frac{Biz}{1+Bi}, \tag{3.6}$$

and noting that when $Bi=0$ a uniform temperature of $T_s=1$ results and hence thermal effects disappear from the problem. The destabilization brought on by the Marangoni effect can be explained by considering a small sinusoidal perturbation on the surface of the fluid layer. At the trough the temperature will be larger than at the crest since it is closer to the heated bottom surface. Thus, surface tension will be weaker at the trough than at the crest resulting in a gradient in surface tension. This, in turn, will cause the fluid to be pulled away from the trough region to the crest region and in doing so will accentuate the perturbation. Lastly, condition (3.4) can also be obtained by considering the first-order Benney equation corresponding to our problem. These details are presented in Appendix A.

To determine how bottom topography alters the instability threshold, we analyse (2.28)–(2.30) using

$$h = h_s(x) + \hat{h}, \quad q = 1 + \hat{q}, \quad \theta = \theta_s(x) + \hat{\theta}, \tag{3.7}$$

where $h_s(x)$ and $\theta_s(x)$ denote the steady-state solutions to (2.29) and (2.30) and satisfy

$$\begin{aligned}&\frac{5\delta^2 We}{6}h_s^3 h_s''' - \frac{6\delta}{Re}h_s h_s'' + \frac{4\delta}{Re}(h_s')^2 - \left[\frac{5\cot\beta}{2Re}h_s^3 + \frac{5\delta}{2Re}\zeta' - \frac{5\delta ReMa}{112}h_s^2\theta_s' - \frac{9}{7}\right]h_s' \\ &\quad - \frac{15\delta}{4Re}\zeta'' h_s - \frac{5Ma}{4}\theta_s' h_s^2 + \left[\frac{15\delta ReMa}{224}\theta_s'' + \frac{5}{2\delta Re} - \frac{5\cot\beta}{2Re}\zeta' + \frac{5\delta^2 We}{6}\zeta'''\right]h_s^3 \\ &\quad = \frac{5}{2\delta Re} + \frac{5\delta}{Re}(\zeta')^2,\end{aligned} \tag{3.8}$$

and

$$\begin{aligned}&\left(\frac{\delta}{RePr} + \frac{3\delta ReMa}{80}h_s(\theta_s-1)\right)h_s^2\theta_s'' + \left[\frac{3\delta ReMa}{40}h_s h_s'(\theta_s-1) + \frac{\delta}{RePr}h_s' - \frac{27}{20}\right]h_s\theta_s' \\ &\quad + \left[\frac{2\delta}{RePr}(h_s')^2 - \frac{3}{\delta RePr}(1+Bih_s) + \frac{3\delta}{RePr}\zeta' h_s' - \frac{\delta}{RePr}\left(\frac{3}{2}\zeta'' + h_s''\right)h_s\right. \\ &\quad \left. - \frac{3Bi\delta}{2RePr}h_s(\zeta'+h_s')^2\right]\theta_s + \frac{3\delta ReMa}{40}h_s^3(\theta_s')^2 = -\frac{3}{\delta RePr} - \frac{\delta}{RePr}h_s\left(\frac{3}{2}\zeta'' + h_s''\right),\end{aligned} \tag{3.9}$$

where the prime refers to differentiation with respect to x. Figures 2 and 3 show some typical steady-state solutions for $h_s(x)$ and $\theta_s(x)$, respectively, whereas the free-surface and bottom contour profiles for this case are illustrated in figure 4. The flattening of the free surface with increasing surface tension is clearly visible. We observed little

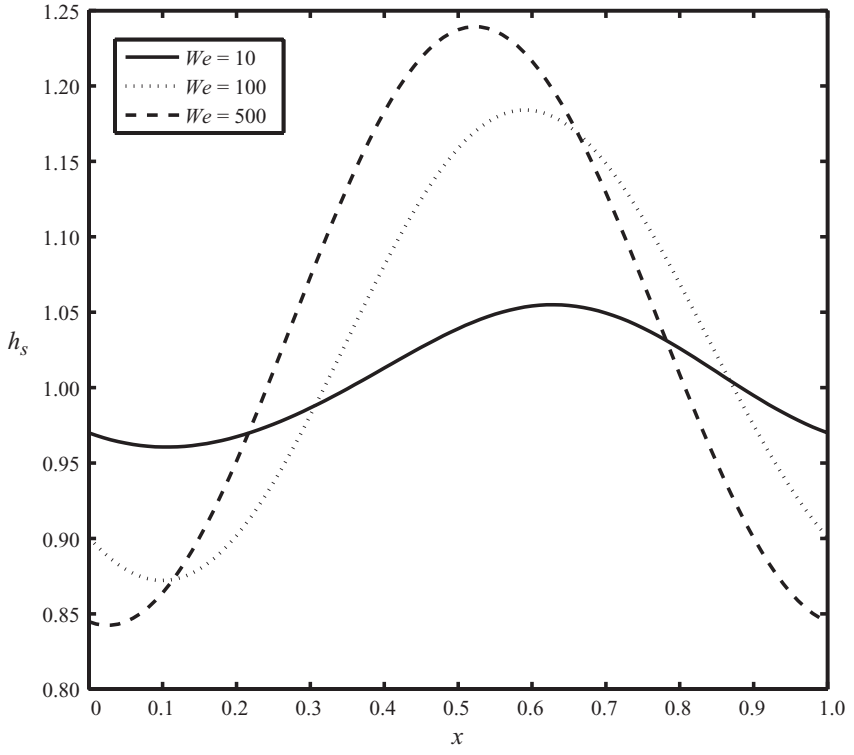

FIGURE 2. Steady-state solution for $h_s(x)$ for the case $Re = 0.5$, $\cot\beta = 0.5$, $\delta = 0.1$, $a_b = 0.2$, $Ma = 1$, $Bi = 1$ and $Pr = 7$ for Weber numbers $We = 10, 100, 500$.

change in the steady-state solution for $h_s(x)$ and $\theta_s(x)$ when going from $We = 500$ to $We = 1000$. Furthermore, the corresponding solutions for $h_s(x)$ for the isothermal case were very similar to those shown with heating applied.

The linearized perturbation equations then become

$$\frac{\partial \hat{h}}{\partial t} + \frac{\partial \hat{q}}{\partial x} = 0, \tag{3.10}$$

$$\frac{\partial \hat{q}}{\partial t} - \frac{9\delta}{2Re}\frac{\partial^2 \hat{q}}{\partial x^2} + f_1\frac{\partial \hat{q}}{\partial x} + f_2\hat{q} + f_3\hat{h} + f_4\frac{\partial \hat{h}}{\partial x} + \frac{6\delta}{Reh_s}\frac{\partial^2 \hat{h}}{\partial x^2} - \frac{5\delta^2 We}{6}h_s\frac{\partial^3 \hat{h}}{\partial x^3} - \frac{5\delta ReMa}{112}h_s'\frac{\partial \hat{\theta}}{\partial x} - \frac{15\delta ReMa}{224}h_s\frac{\partial^2 \hat{\theta}}{\partial x^2} - \frac{\delta ReMa}{48}h_s^2\frac{\partial^2 \hat{\theta}}{\partial x \partial t} = 0, \tag{3.11}$$

$$\frac{\partial \hat{\theta}}{\partial t} + g_1\frac{\partial^2 \hat{\theta}}{\partial x^2} + g_2\frac{\partial \hat{\theta}}{\partial x} + g_3\hat{\theta} + \frac{27\theta_s'}{20h_s}\hat{q} + g_4\hat{h} - \frac{7(1-\theta_s)}{40h_s}\frac{\partial \hat{q}}{\partial x} + g_5\frac{\partial \hat{h}}{\partial x} - \frac{\delta(1-\theta_s)}{RePrh_s}\frac{\partial^2 \hat{h}}{\partial x^2} = 0, \tag{3.12}$$

where the coefficients $f_1(x) - f_4(x)$, $g_1(x) - g_5(x)$ in (3.11) and (3.12) are listed in Appendix B. For periodic bottom topography, these coefficients will also be periodic functions. This permits the use of Floquet–Bloch theory to conduct the stability analysis. We thus represent the perturbations as Bloch-type functions having the

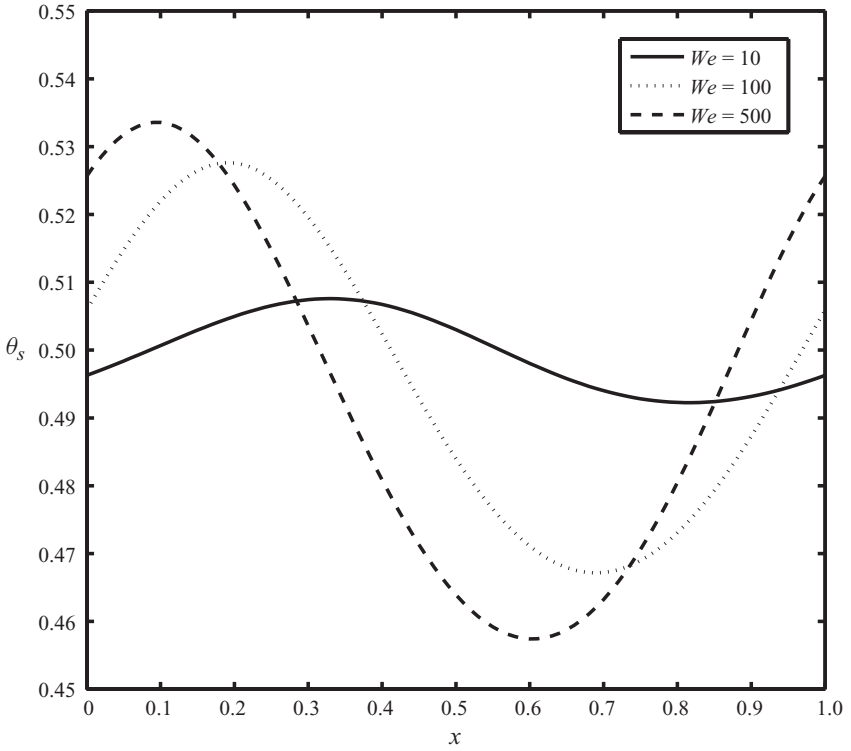

FIGURE 3. Steady-state solution for $\theta_s(x)$ for the case $Re = 0.5$, $\cot\beta = 0.5$, $\delta = 0.1$, $a_b = 0.2$, $Ma = 1$, $Bi = 1$ and $Pr = 7$ for Weber numbers $We = 10, 100, 500$.

form

$$\hat{h} = \mathrm{e}^{\sigma t}\mathrm{e}^{iKx}\sum_{n=-\infty}^{\infty}\hat{h}_n\mathrm{e}^{\mathrm{i}2\pi nx}, \quad \hat{q} = \mathrm{e}^{\sigma t}\mathrm{e}^{\mathrm{i}Kx}\sum_{n=-\infty}^{\infty}\hat{q}_n\mathrm{e}^{\mathrm{i}2\pi nx}, \quad \hat{\theta} = \mathrm{e}^{\sigma t}\mathrm{e}^{\mathrm{i}Kx}\sum_{n=-\infty}^{\infty}\hat{\theta}_n\mathrm{e}^{\mathrm{i}2\pi nx}. \tag{3.13}$$

The exponential factor containing the Bloch wavenumber, K, represents disturbances which interact with the periodic bottom topography via the equilibrium flow, which is represented by the Fourier series composed of its harmonics. Introducing the Bloch-type functions with truncated series into the perturbation equations reduces the equations to an algebraic problem, which can be solved numerically for the temporal growth rate $\Re(\sigma)$. In this way, we can determine the critical Reynolds number for the onset of instability, and for supercritical flows, we can compute the wavelength and speed of unstable disturbances.

In order to reduce the parameter space to a manageable dimension, we have kept the Prandtl number fixed at $Pr = 7$, which corresponds to water at room temperature. In most of our results, the Biot number was also fixed at $Bi = 1$. To establish the impact of the remaining parameters Ma, We, $\cot\beta$, a_b and δ on the stability of the flow for an uneven bottom, we start by presenting distributions of the critical Reynolds number, Re_{crit}, with bottom amplitude for $We = 10, 50, 450$ in figures 5–7. These figures clearly reveal that Re_{crit} depends on surface tension and this marks an important distinction in the stability characteristics between even and uneven surfaces, since for an even bottom Re_{crit} is independent of We. Another interesting

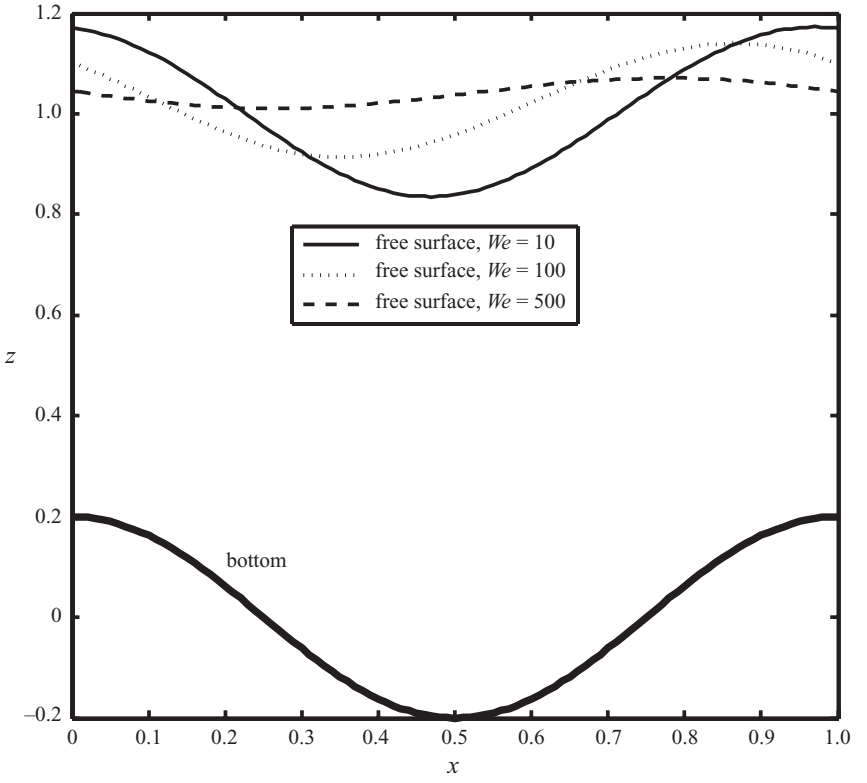

FIGURE 4. Free surface and bottom contour for the case $Re = 0.5$, $\cot\beta = 0.5$, $\delta = 0.1$, $a_b = 0.2$, $Ma = 1$, $Bi = 1$ and $Pr = 7$ for Weber numbers $We = 10, 100, 500$.

feature, illustrated in figures 5–7, is that for the range $0 \leqslant a_b \leqslant 0.5$ the entire Re_{crit} distribution lies either above or below the value associated with the even bottom, Re_{crit}^{even}. Thus, for a fixed Weber number, the influence of bottom topography on the stability of the flow does not depend on the amplitude. It does, however, depend on Ma and $\cot\beta$ as portrayed in figures 5–7.

In figure 5, the complicated interaction between surface tension and bottom topography is displayed for the case $Ma = 1$ and $\cot\beta = 1$. We see that for $We = 10$ and $We = 50$ bottom topography plays a stabilizing role while for $We = 450$ it has a destabilizing influence. Increasing the Marangoni number to $Ma = 5$, shown in figure 6, we notice that for a fixed We the Re_{crit} distribution lies below the corresponding one for $Ma = 1$. This leads to the general conclusion that increasing Ma has a destabilizing influence as it was found for the even bottom case. On the other hand, we also observe that for $Ma = 5$ bottom topography plays a stabilizing role, since for the Weber numbers presented the distribution lies above the value Re_{crit}^{even}, which is not the case for $Ma = 1$. However, soon we will show that for $Ma = 5$ bottom topography also plays a destabilizing role if the Weber number is sufficiently large. Comparing figures 5 and 7, it is seen that the influence that bottom topography has on the stability for large Weber numbers depends on the inclination. As the inclination is increased, bottom topography has a stabilizing role for large-Weber-number flows. Lastly, the values of Re_{crit} as $a_b \to 0$ in figures 5–7 are in excellent agreement with

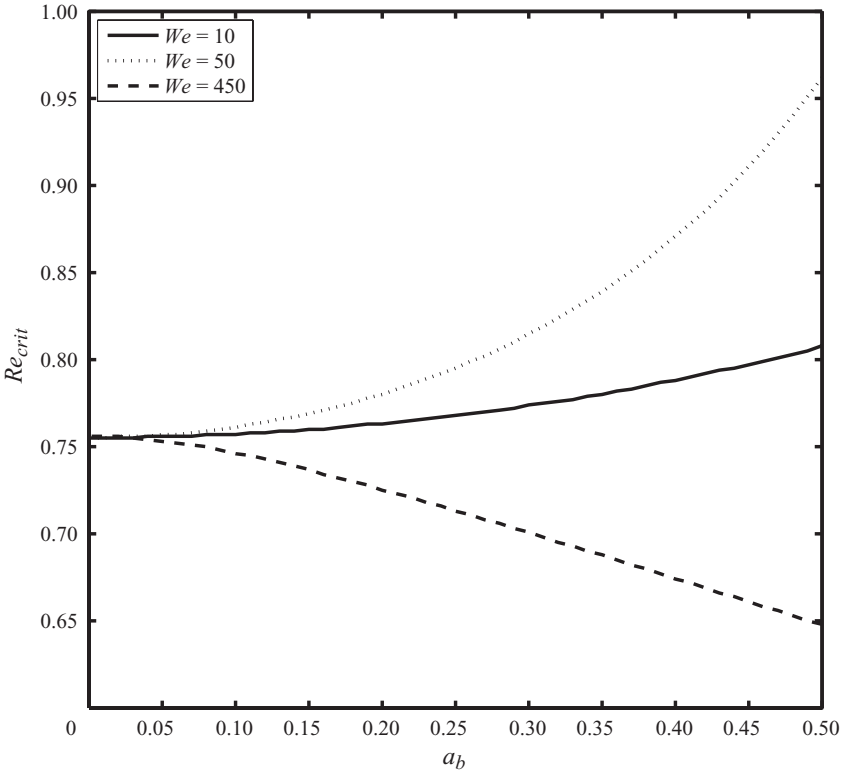

FIGURE 5. Critical Reynolds number as a function of bottom amplitude with $\delta = 0.05$, $\cot\beta = 1$, $Ma = 1$, $Bi = 1$ and $Pr = 7$.

those predicted by (3.4). As expected, these results are independent of We and the figures clearly reveal this.

To establish the impact of heating and the Marangoni effect on the stability of the flow, in figure 8 we first present a plot of the critical Reynolds number versus the Marangoni number for $We = 10, 50, 450$. This diagram reaffirms the claim that the Marangoni effect appears to have a destabilizing influence on the flow. A similar plot of Re_{crit} with Bi, which is shown in figure 9, demonstrates that there is a minimum at $Bi = 1$ as in the even bottom case.

In figures 10 and 11, we fix the bottom amplitude and set $a_b = 0.2$. Since we have discovered that surface tension influences the instability threshold, for ease of interpretation we have decided to plot $(Re_{crit}^{even} - Re_{crit})$ versus We for $\delta = 0.05, 0.07, 0.1$ with the understanding that $(Re_{crit}^{even} - Re_{crit}) > 0$ denotes a destabilizing effect on the flow by bottom topography while $(Re_{crit}^{even} - Re_{crit}) < 0$ indicates that bottom topography plays a stabilizing role. Values of We, where $(Re_{crit}^{even} - Re_{crit}) = 0$, can be regarded as transition points since the action of bottom topography as a stabilizing or destabilizing agent reverses as We passes through these values. Indeed, the reversal in stability as We increases is also evident from figure 5.

A reversal in the stabilizing action of bottom topography for the isothermal case has been reported by D'Alessio *et al.* (2009) and Heining & Aksel (2009), and is also apparent in the results reported by Häcker & Uecker (2009). Heining & Aksel (2009) investigate the inverse problem, while Häcker & Uecker (2009) address the direct problem and express the equations of motion in terms of curvilinear coordinates

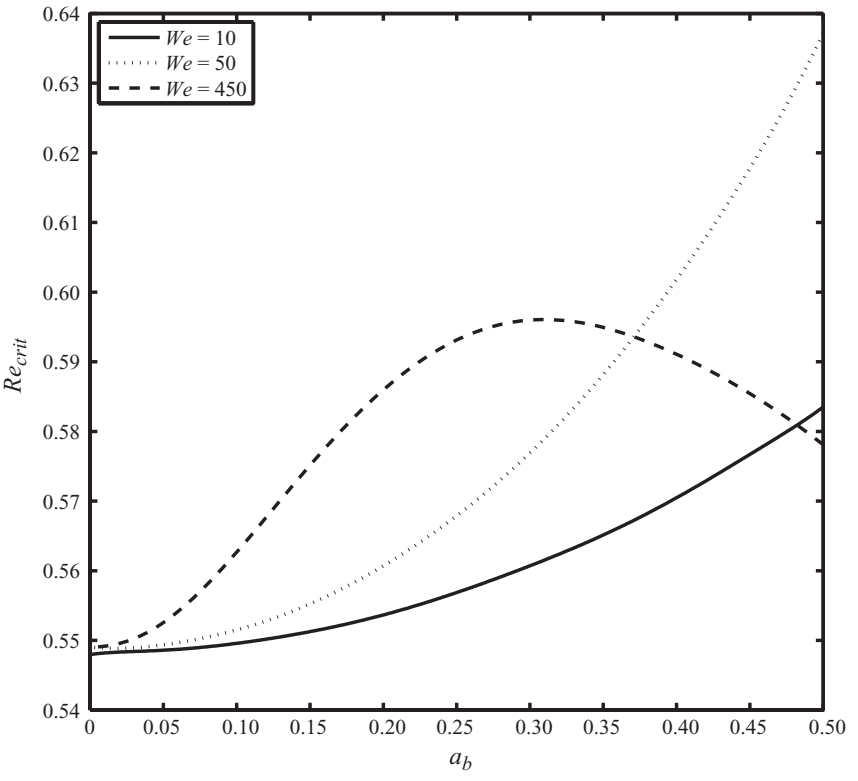

FIGURE 6. Critical Reynolds number as a function of bottom amplitude with $\delta = 0.05$, $\cot\beta = 1$, $Ma = 5$, $Bi = 1$ and $Pr = 7$.

relative to the bottom profile. As was done by D'Alessio *et al.* (2009), Häcker & Uecker (2009) then resort to the weighted residual approach and implement a Galerkin method with a single-function expansion; however, in doing so they utilize a more refined velocity profile as was proposed by Scheid, Ruyer-Quil & Manneville (2006). The effect of surface tension on the stability of the flow is not the focus of the investigation reported by Häcker & Uecker (2009), and only three different values of the relevant parameter are considered. Nevertheless, examining the presented critical Reynolds number distributions with the bottom waviness, it is evident that a reversal in the stabilizing role played by bottom topography is indicated as the surface-tension parameter is increased. It should be pointed out that in all of these previous investigations, only small to moderate surface tension is considered. To the best of our knowledge, the current work is the first investigation to consider a large range ($10 \leqslant We \leqslant 10^5$) of surface-tension values, and to discover a complicated non-monotonic variation of the critical Reynolds number with this parameter.

Figure 10, which contains results for the isothermal case, reveals that for small We values bottom topography acts to stabilize the flow, while for sufficiently large We values the role played by surface tension reverses to a destabilizing one. In the intermediate range, there is strong dependence on We with large deflections of the curves from zero, indicating a significant influence of bottom topography on flow stability, particularly around the transition point. It should also be pointed out that, since Re_{crit}^{even} is independent of We, intervals of increase and decrease of the $(Re_{crit}^{even} - Re_{crit})$ curve correspond to intervals of decrease and increase of Re_{crit},

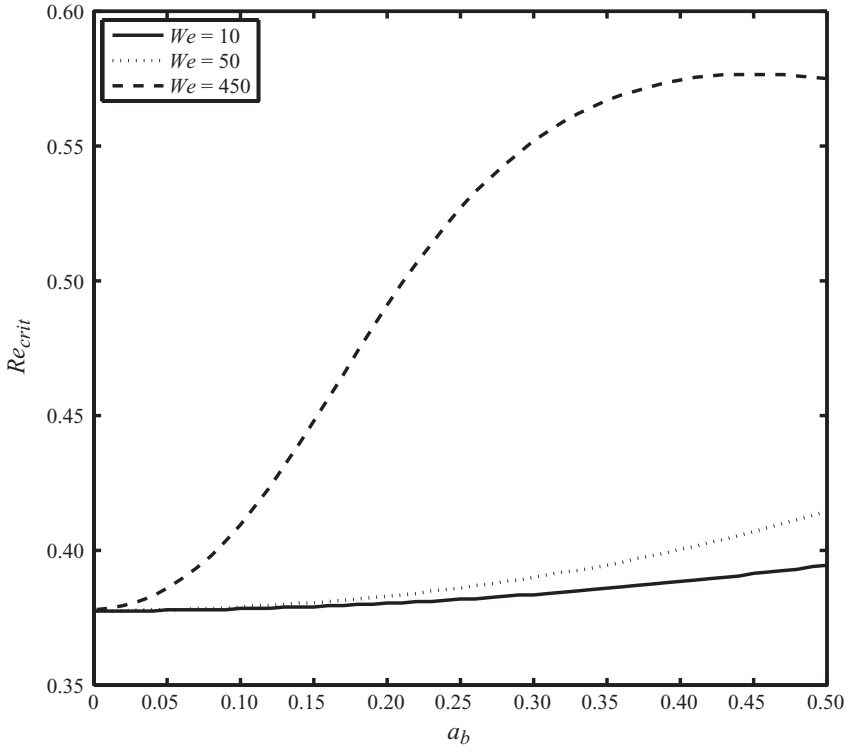

FIGURE 7. Critical Reynolds number as a function of bottom amplitude with $\delta = 0.05$, $\cot\beta = 0.5$, $Ma = 1$, $Bi = 1$ and $Pr = 7$.

respectively. So, the turning (or stationary) points on these curves signal a reversal in the stabilizing (or destabilizing) role played by surface tension.

The effect of decreasing δ, as can be seen in figure 10, is to increase the We value of the transition point. Now, based on our scaling, decreasing δ can be associated with increasing the wavelength of the bottom topography. Hence we can infer that for longer bottom undulations stronger surface tension is needed to effectuate the more significant coupling between surface tension and bottom unevenness. The $(Re_{crit}^{even} - Re_{crit})$ curves corresponding to the non-isothermal case presented in figure 11 have the same general shape as their isothermal counterparts, with the same number of transition and turning points. A close examination, however, reveals that heating increases the value of the transition Weber number and diminishes the effect that bottom topography has on the stability of the flow for the entire We range.

In figure 12, we present the $(Re_{crit}^{even} - Re_{crit})$ distributions with We for various $\cot\beta$ values with $\delta = 0.1$. It can be seen that as $\cot\beta$ is increased a larger portion of the distribution lies above zero, which points to the fact that decreasing the inclination accentuates the destabilizing influence of bottom topography. Figure 13 shows a plot of $(Re_{crit}^{even} - Re_{crit})$ versus We for $a_b = 0.1, 0.2, 0.4$. All the curves have approximately the same transition point. There is, however, a difference in the deviations from Re_{crit}^{even}: the smaller the bottom amplitude the smaller the deviations. Lastly, we present the Re_{crit} distribution with a_b for $Ma = 1, 5$ in figure 14. The curves indicate that in the presence of sufficiently strong surface-tension thermocapillary effects can cause an

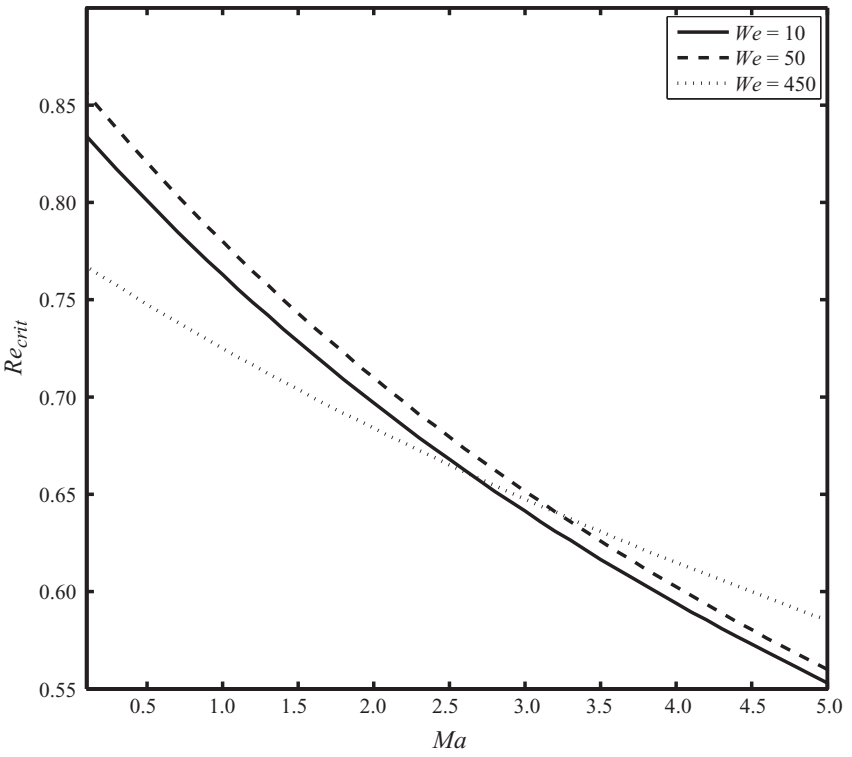

FIGURE 8. Critical Reynolds number as a function of Marangoni number with $a_b = 0.2$, $\delta = 0.05$, $\cot\beta = 1$, $Bi = 1$ and $Pr = 7$.

abrupt change in the critical Reynolds number. Indeed, a reversal in stability occurs when the Marangoni number is increased from $Ma = 1$ to $Ma = 5$ as a result of bottom unevenness coupled with strong surface tension. One last observation worth noting regards the profile of the steady-state free surface in relation to that of the bottom. For small Weber numbers, apart from a vertical shift, the free-surface profile mirrors that of the bottom. However, as We increases the two profiles become out of phase. In fact, the shift between profiles seems to develop near the occurrence of the reversal in stability. As We increases further the free surface becomes flatter but still noticeably out of phase with the bottom. This behaviour was observed in all cases and is apparent in figure 4.

As a final plot, figure 15 presents neutral stability curves in the $K - Re$ plane for different bottom amplitudes and Marangoni numbers. The interesting feature observed here is that for small a_b the critical wavenumber occurs at $K = 0$. That is, perturbations having an infinitely long wavelength are the most unstable. However, for larger a_b the critical wavenumber moves away from $K = 0$, and the neutral stability curve takes on a significantly different shape. As evident from the diagram, the Marangoni number also influences the shape of the curve.

In the next section, we present numerical simulations and comparisons to validate our modelling equations and also to verify some of the predictions made in this section. Because of the lack of experimental data available for heated falling films, our focus will be on isothermal flows.

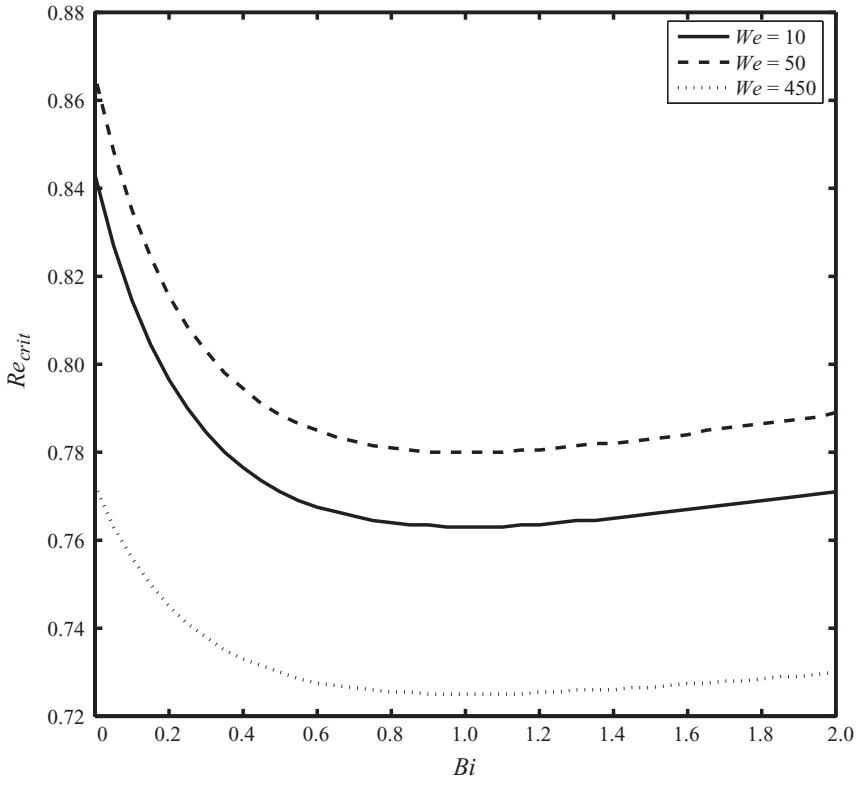

FIGURE 9. Critical Reynolds number as a function of Biot number with $a_b = 0.2$, $\delta = 0.05$, $\cot\beta = 1$, $Ma = 1$ and $Pr = 7$.

4. Results, comparisons and discussions

The instability of a particular equilibrium flow can be determined by gauging the evolution initiated by small disturbances. The development of the flow can be calculated by numerically solving the fully nonlinear governing equations. The advantage of this approach is that it incorporates nonlinear interactions of the perturbations and thus captures the entire instability mechanism of the flow. Furthermore, for unstable flows, the temporal evolution can be continued until the growth of the disturbances reaches saturation with the solution then revealing the structure of the subsequent secondary flow. Using this numerical approach to perform a nonlinear stability analysis has been successful in related previous studies (Kranenburg 1992; Brook, Pedley & Falle 1999; Chang, Demekhin & Kalaidin 2000; Zanuttigh & Lamberti 2002; Balmforth & Mandre 2004; D'Alessio *et al.* 2009).

We employed the numerical method described in Appendix C to solve the governing unsteady equations (2.28)–(2.30) on a periodic spatial domain of length L, where L is some multiple of the bottom wavelength. The evolution of the unsteady flow was computed using the perturbed steady-state solutions as initial conditions. Since the computational domain length, L, forces the largest wavelength (smallest wavenumber) of the perturbation to be L (wavenumber $2\pi/L$), we can thus exploit this feature to determine the critical Reynolds number for which the flow becomes unstable by varying Re for a fixed L using a perturbation of wavelength L. Using this strategy, we ran numerous numerical simulations to identify points on the neutral stability

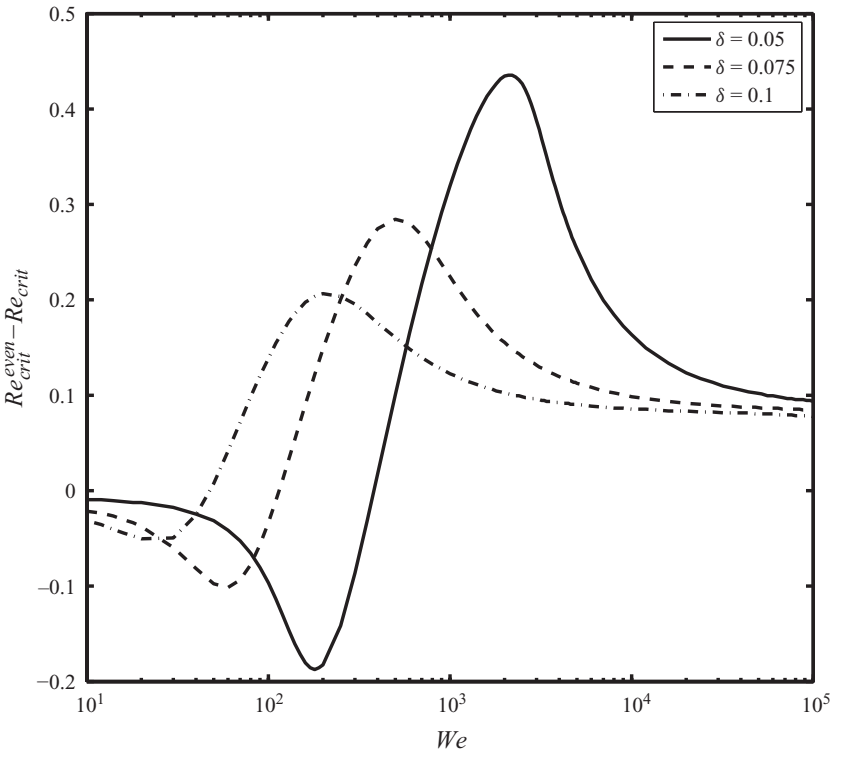

FIGURE 10. Critical Reynolds number as a function of Weber number with $a_b = 0.2$, $\cot\beta = 1$ for the isothermal case.

curve. Figure 16 shows a comparison in the $K - Re$ plane between these points and the theoretical curve obtained using the linear analysis of the previous section. The figure displays close agreement between the nonlinear simulations and linear theory.

We next make comparisons with experimental data and begin with the isothermal case over an even bottom. For this, we refer to the experiments conducted by Liu *et al.* (1995) using glycerin–water films at an inclination of $\beta = 4.0°$. The fluid properties corresponding to their set-up are as follows:

$$\nu = 2.3 \times 10^{-6} \frac{\mathrm{m}^2}{\mathrm{s}}, \quad \rho = 1.07 \times 10^3 \frac{\mathrm{kg}}{\mathrm{m}^3}, \quad \sigma_0 = 6.7 \times 10^{-2} \frac{\mathrm{N}}{\mathrm{m}}. \tag{4.1}$$

Their data consist of points on the neutral stability curve in the $f - Re$ plane, where f denotes the cutoff frequency. The following expression for the neutral stability curve can easily be derived using a linear stability analysis and is given by

$$\frac{5}{6}\frac{\cot\beta}{Re} = \frac{175 + 5(\delta k)^2 - 33(\delta k)^4}{7[5 + 9(\delta k)^2]^2} - \frac{5}{18} We(\delta k)^2. \tag{4.2}$$

Figure 17 illustrates a comparison between the two in the $\delta k - Re$ plane, where δk and f are related through

$$f = \left(\frac{g \sin\beta}{3}\right)^{2/3} \left(\frac{Re}{\nu}\right)^{1/3} \frac{c\delta k}{2\pi}. \tag{4.3}$$

The critical Reynolds numbers from the experimental data have been scaled by 2/3 so as to conform with our definition of Re. In arriving at the above expression, we

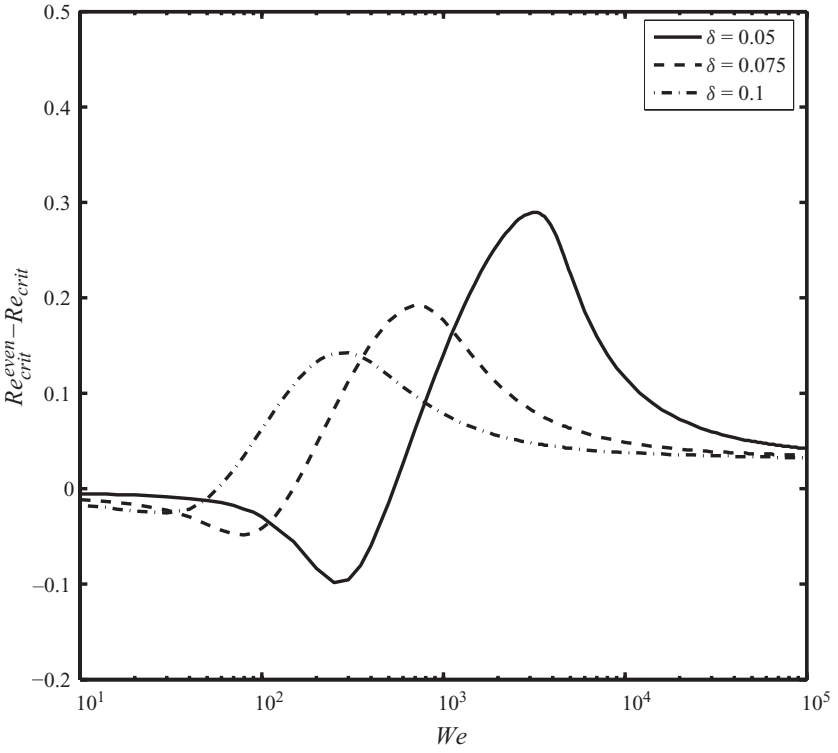

FIGURE 11. Critical Reynolds number as a function of Weber number with $a_b = 0.2$, $\cot\beta = 1$, $Ma = 5$, $Bi = 1$ and $Pr = 7$.

have made use of the scaling introduced earlier with c denoting the dimensionless phase speed and f is in Hz. Since the fluid is specified the Weber number in (4.2) can be expressed as

$$We = \left(\frac{3}{\sin\beta}\right)^{1/3} \frac{Ka}{Re^{5/3}}, \tag{4.4}$$

where $Ka = \sigma_0/(\rho g^{1/3}\nu^{4/3})$ denotes the Kapitza number. Since Ka depends only on the fluid properties it has a numerical value of $Ka = 963.45$. Figure 17 displays very good agreement between experimental and theoretical values.

For the isothermal case of an uneven bottom, the only experimental data available are those of Wierschem *et al.* (2005). The fluid used in their experiments is a silicone oil (B200) having the following fluid properties:

$$\nu = 2.24 \times 10^{-4}\frac{\mathrm{m}^2}{\mathrm{s}}, \quad \rho = 9.68 \times 10^{2}\frac{\mathrm{kg}}{\mathrm{m}^3}, \quad \sigma_0 = 2.07 \times 10^{-2}\frac{\mathrm{N}}{\mathrm{m}}. \tag{4.5}$$

The experimental apparatus had a wavy bottom consisting of three equal sinusoidal waves having

$$\frac{A_b}{\lambda_b} = 0.05. \tag{4.6}$$

Table 1 shows a comparison between the experimental, numerical and theoretical Re_{crit} values. The numerical results were obtained by solving our nonlinear model equations with a disturbance of wavelength L added to the steady-state solutions. By monitoring the growth or decay of the disturbance and stepping the Reynolds

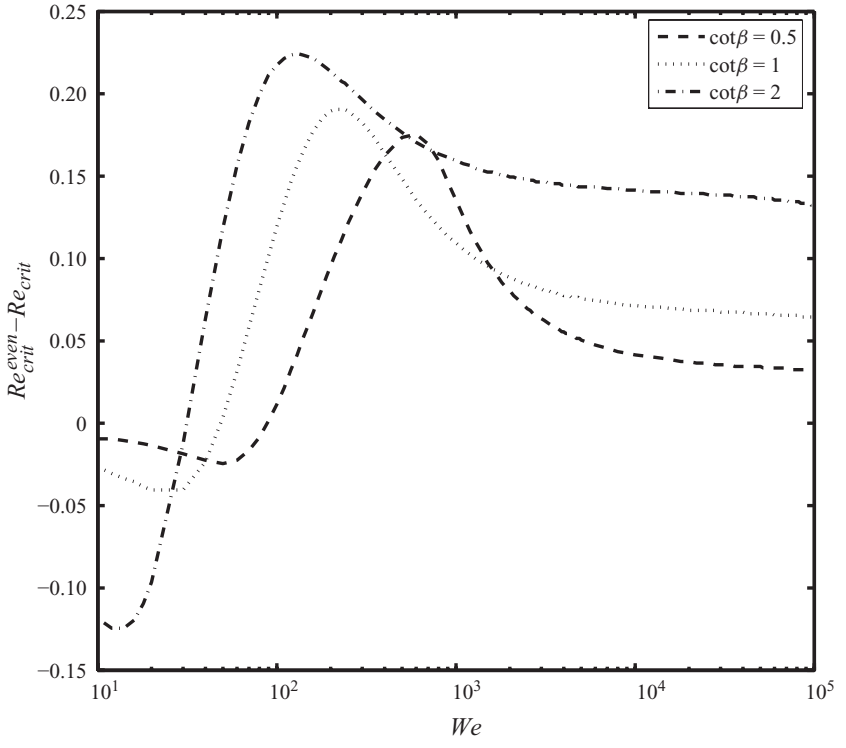

FIGURE 12. Critical Reynolds number as a function of Weber number with $a_b = 0.2$, $\delta = 0.1$, $Ma = 1$, $Bi = 1$ and $Pr = 7$.

number in increments of 0.1, we were able to determine the interval over which the flow changed from being stable to becoming unstable. Initially, we solved the equations on a domain having a length of $L = 3$, which corresponds to three bottom wavelengths as in the experiments. On physical grounds, we expect the results to be independent of L, and thus we increased L until the results converged. We found that using $L = 10$ was more than sufficient to guarantee convergence. The observed trend was that the critical Reynolds number decreased slightly as L increased. Based on the fluid properties and set-up, the Weber number as defined in this study was very small. For example, with $a_b = 0.5$ and $\delta = 0.1$ the range in We was $9.7 \times 10^{-7} \leqslant We \leqslant 6.2 \times 10^{-5}$ for the three inclinations used in the experiments. In selecting the parameters a_b and δ, we need to satisfy the condition

$$\frac{A_b}{\lambda_b} = a_b \delta = 0.05. \tag{4.7}$$

Table 1 corresponds to the case $a_b = 0.5$ and $\delta = 0.1$. The theoretical values listed in this table refer to those obtained from our linear stability analysis using Floquet–Bloch theory. The agreement between numerical and experimental values is quite reasonable; the numerical values lie just outside the error bars. We found that the agreement improved for other choices of a_b and δ. For example, with $a_b = 1$ and $\delta = 0.05$ we obtained $5.3 < Re_{crit} < 5.4$ (i.e. $Re_{crit} \in (5.3, 5.4)$) for the inclination $\beta = 15°$. The agreement between numerical and theoretical values, on the other hand, is very good.

		Re_{crit}		
β	Re_{crit}^{even}	Experimental	Numerical	Theoretical
15°	3.1	5.1 ± 0.4	(5.5, 5.6)	5.6
30°	1.4	2.2 ± 0.2	(1.8, 1.9)	1.7
40.7°	0.97	1.3 ± 0.1	(1.1, 1.2)	1.1

TABLE 1. Comparison between experimental, numerical and theoretical values of Re_{crit} for the isothermal case having $a_b = 0.5$ and $\delta = 0.1$.

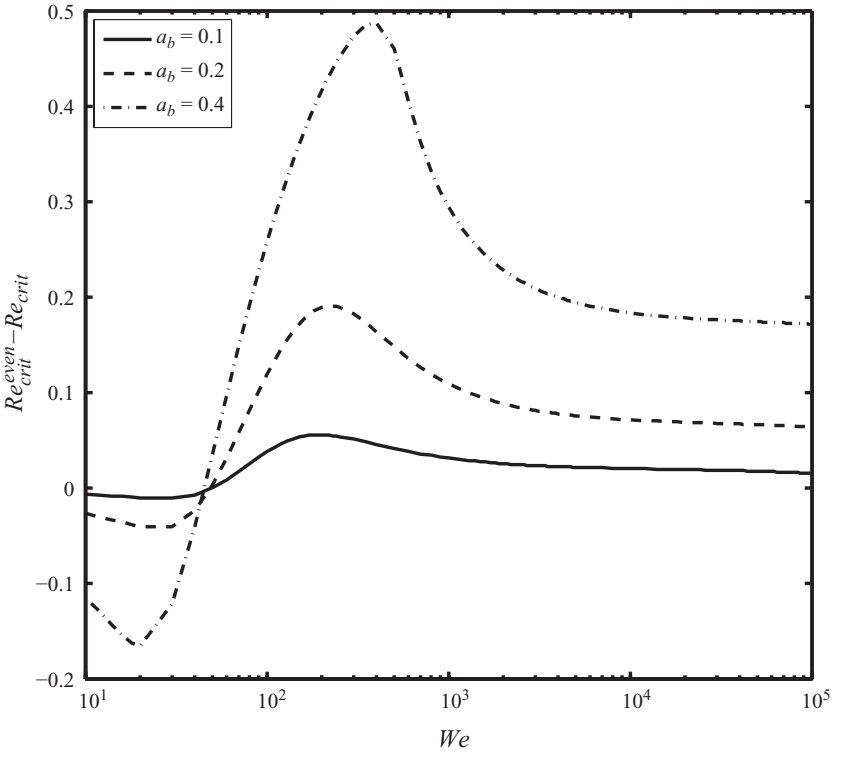

FIGURE 13. Critical Reynolds number as a function of Weber number with $\delta = 0.1$, $\cot\beta = 1$, $Ma = 1$, $Bi = 1$ and $Pr = 7$.

Here, $Re_{crit}^{even} = 5\cot\beta/6$ refers to the critical Reynolds number for the even bottom case and is included to illustrate the stabilizing influence of bottom topography. Lastly, we note that the critical Reynolds numbers presented in the experimental investigation of Wierschem *et al.* (2005) were multiplied by 2/3 in order to comply with our definition of Re.

Numerical simulations, as outlined above, were also used to confirm the reversals in stability as predicted by linear theory. For example, linear theory predicts that for the isothermal case having $a_b = 0.5$, $\delta = 0.1$ and $\cot\beta = 0.5$, $Re_{crit} > Re_{crit}^{even}$ when $We = 10$, while $Re_{crit} < Re_{crit}^{even}$ when $We = 100$. With $Re = Re_{crit}^{even}$, numerical simulations revealed that disturbances decayed in time when $We = 10$ and grew in time when $We = 100$.

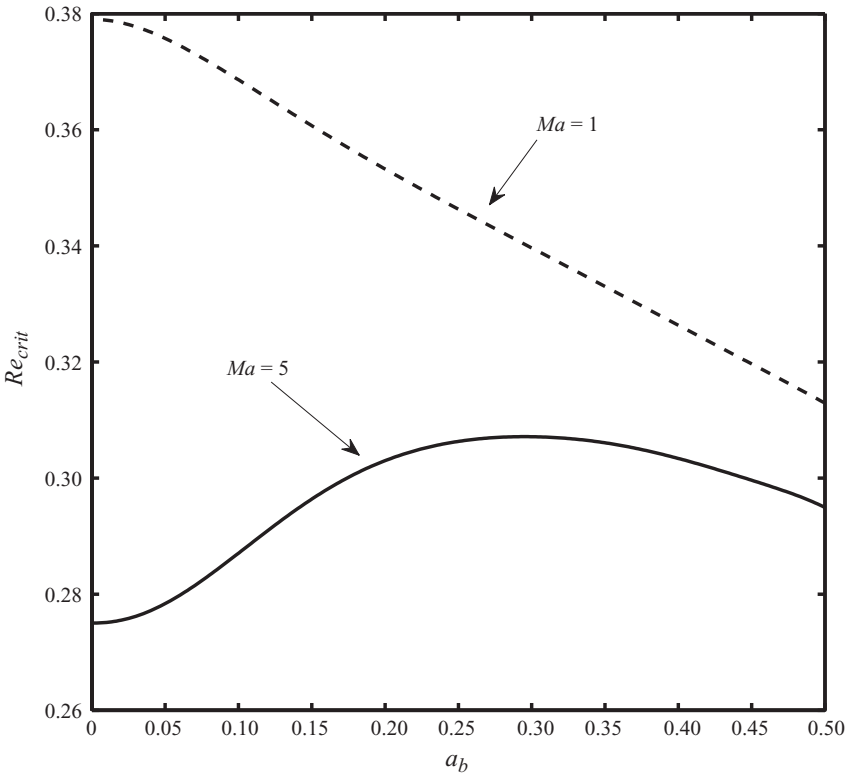

FIGURE 14. Critical Reynolds number as a function of bottom amplitude with $\delta = 0.05$, $\cot\beta = 0.5$, $We = 900$, $Bi = 1$ and $Pr = 7$.

Next, we make comparisons with direct numerical simulations utilizing the software package CFX. This program solves the Navier–Stokes equations, expressed in terms of the primitive variables u, v, w and p, using a combination of the finite volume and finite element methods. The domain is discretized into fluid elements and control volumes are formed around element nodes with momentum and mass being conserved over each control volume. Flow variables and fluid properties are stored at the nodes, which are located within each control volume. The finite element method, using shape functions, is employed to calculate properties within fluid elements at the edges of the control volumes. An advection discretization scheme is used which is a bounded second-order upwind scheme. To locate the free surface, a volume-of-fluid method is used. The volume fraction of fluid is tracked as a solution variable using a volume fraction advection scheme. This causes a smearing of the interface due to numerical diffusion; however, CFX uses a compressive scheme to minimize this diffusion. The interface location in this study was chosen as the contour along which the volume fractions of water and air are each 0.5.

In our two-dimensional simulations, a domain length of 20 bottom wavelengths (i.e. $L = 20$) was chosen with periodic boundary conditions applied at the ends, and steady-state solutions used as initial conditions. We have found that the progression of an unstable flow mimics the general phases observed in isothermal film flows (Chang, 1994), and shallow flows along even (Brock 1969; Julien & Hartley 1986) and uneven (D'Alessio *et al.* 2009) surfaces. Figure 18 presents comparisons between our model and CFX simulations for a supercritical isothermal case at a dimensionless time

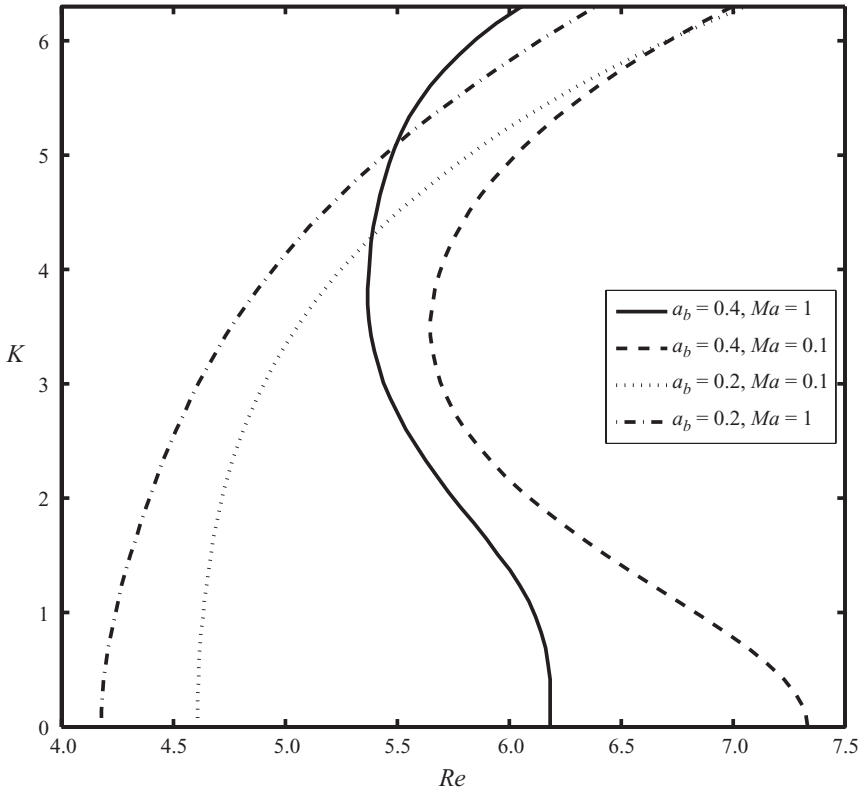

FIGURE 15. Neutral stability curves for the case $\delta = 0.05$, $\cot\beta = 5$, $We = 5$, $Bi = 1$ and $Pr = 7$.

of $t = 137$. In terms of dimensional units, the flow set-up for the CFX simulations corresponds to a configuration having a bottom wavelength of $\lambda_b = 1$ mm and amplitude $A_b = 0.01$ mm and Nusselt thickness $H = 0.1$ mm. The figure shows that with the passage of time an initially constant distribution for q eventually settles into a permanent wave profile consisting of three peaks. The agreement between the two simulations is good; our model is able to correctly predict the essential features. The only noticeable difference is in the spacing between the peaks. Similar agreement in the free-surface profile is also found. We observe that apart from the three prominent waves the free-surface variations appear to be in phase with the bottom undulations, as previously noted for cases with weak surface tension.

As a final simulation, we consider a non-isothermal supercritical case with moderately strong surface tension. Figures 19–21 present plots obtained from our model equations. Figure 19 shows how a perturbed initial steady-state solution evolves in time to form a permanent solitary wave structure. In figure 20, the corresponding distributions for the fluid thickness, h, and fluid surface temperature, θ, are plotted at $t = 200$. We observe that the surface temperature distribution is out of phase with that of h indicating that a thinner fluid layer results in a larger surface temperature. This can be reasoned by examining the steady-state temperature profile given by

$$T_s(x, z) = 1 - \frac{Bi}{(1 + Bi)h_s(x)}(z - \zeta(x)). \tag{4.8}$$

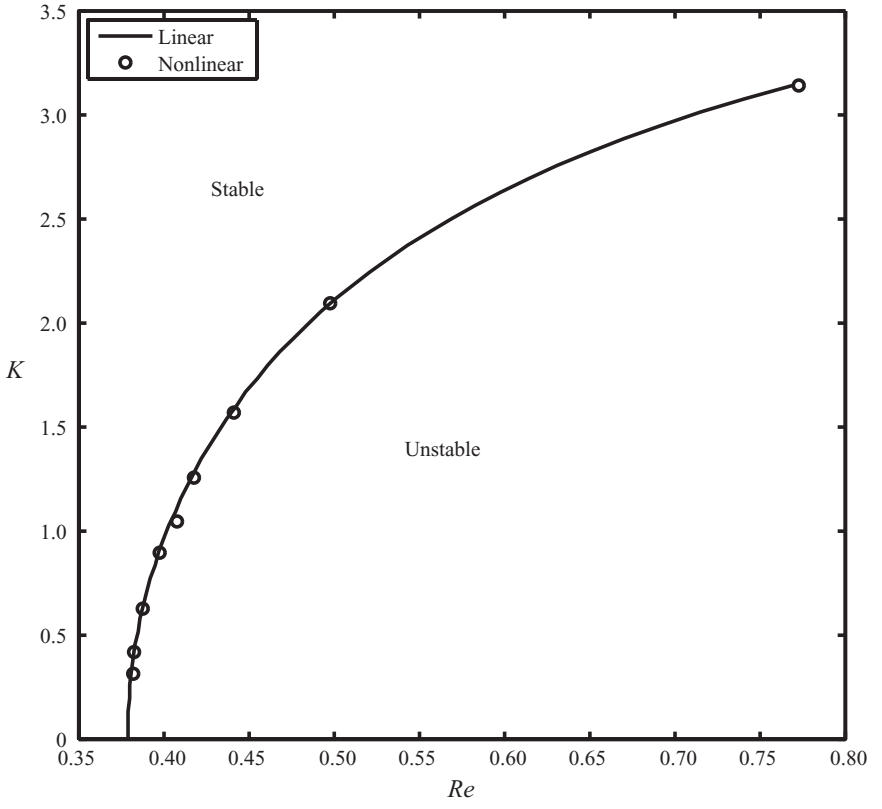

FIGURE 16. Neutral stability curve for the case $a_b = 0.1$, $\delta = 0.1$, $\cot\beta = 0.5$, $We = 10$, $Ma = 1$, $Bi = 1$ and $Pr = 7$.

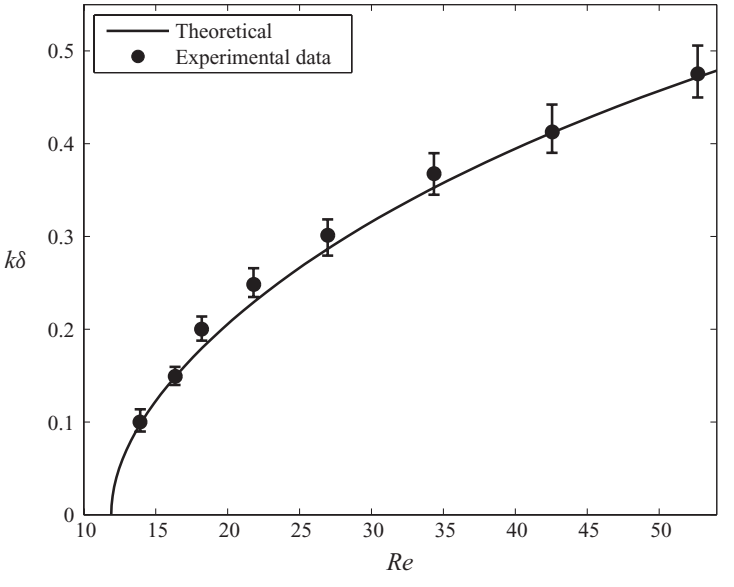

FIGURE 17. Comparison between experimental and theoretical neutral stability curves for the isothermal case with $a_b = 0$, $\beta = 4.0°$ and $Ka = 963.45$.

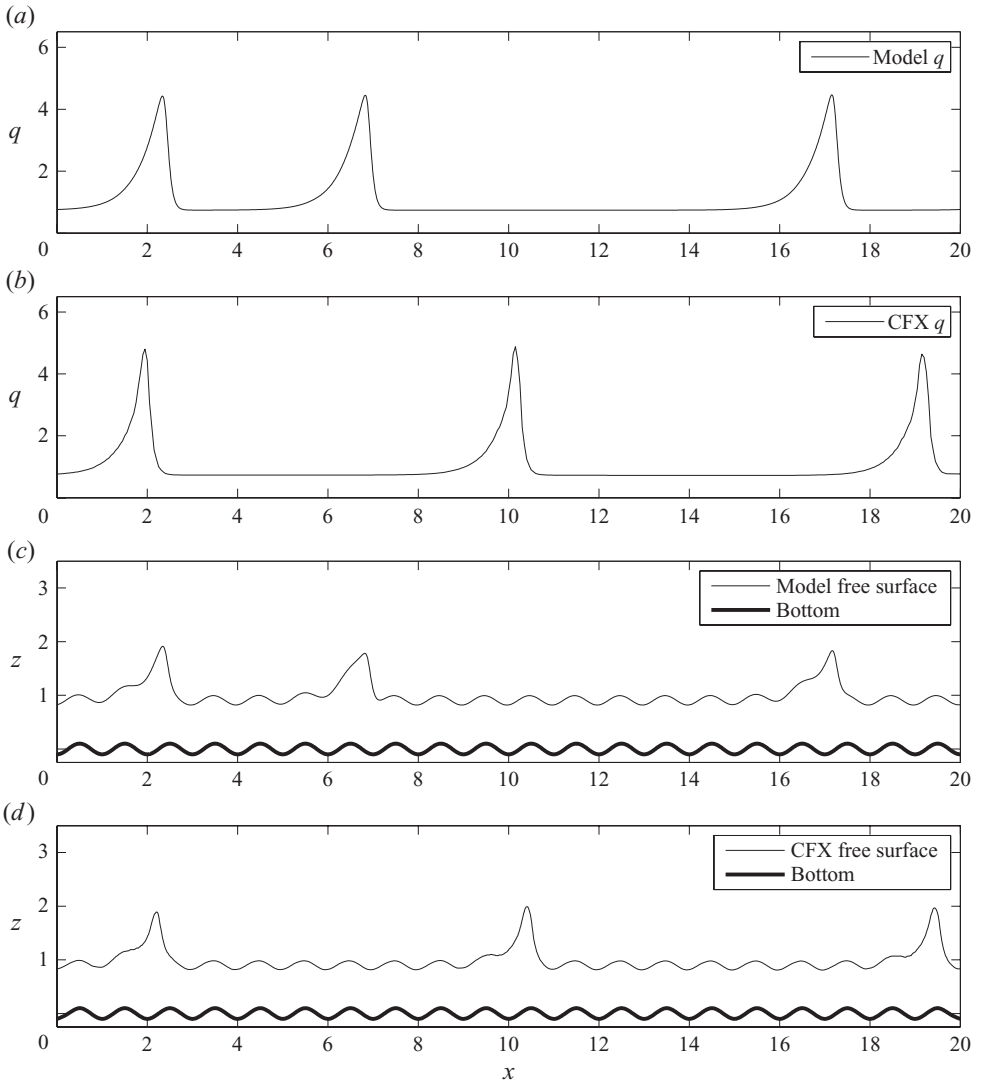

FIGURE 18. Comparison in the permanent q and free-surface profiles for the isothermal case with $Re = 2.28$, $\cot\beta = 1.5$, $We = 0$, $a_b = 0.1$ and $\delta = 0.1$ on a computational domain of length $L = 20$.

This shows that the temperature decreases from the bottom surface at a uniform rate, which depends only on the heat transfer coefficient, Bi, and we expect a similar behaviour to occur for the unsteady case as well. Lastly, figure 21 displays the free-surface profile at $t = 200$, which illustrates how the free-surface variations become out of phase with the bottom topography in the presence of sufficiently strong surface tension.

In an attempt to understand the interaction between bottom topography and surface tension, we begin by constructing an approximate steady-state solution of the two-dimensional equations (2.4)–(2.6). Since we have demonstrated that the reversals in stability occur with or without heating, for simplicity we consider the isothermal case. We start by expanding the steady-state flow variables u_s, w_s, p_s and h_s in the

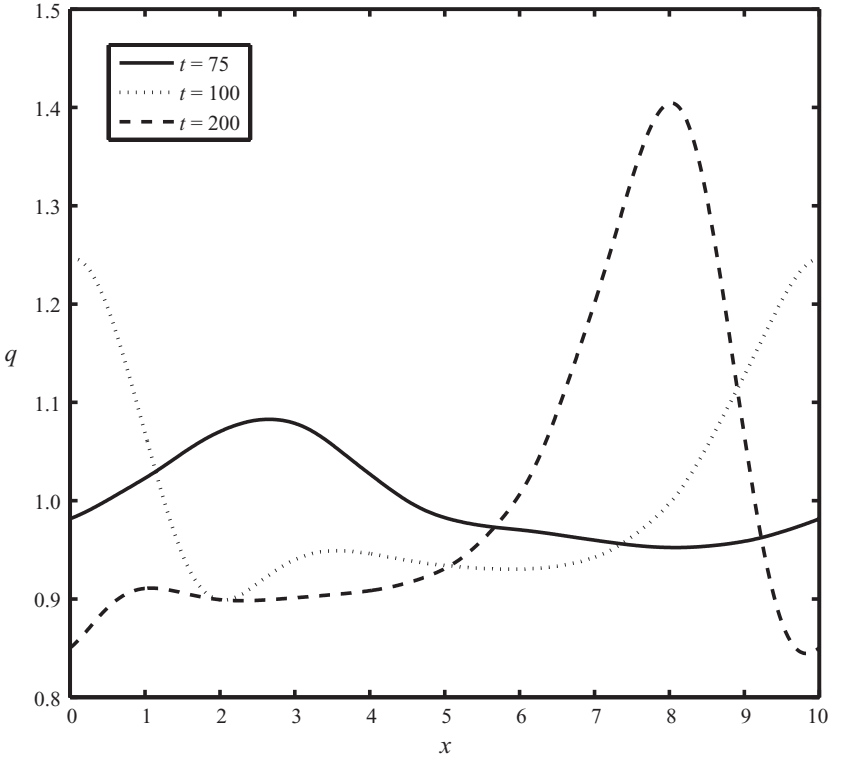

FIGURE 19. Evolution of the q distribution for the case with $Re = 1$, $\cot\beta = 0.5$, $Bi = 1$, $Ma = 1$, $We = 100$, $a_b = 0.2$, $\delta = 0.1$ and $Pr = 7$ on a computational domain of length $L = 10$.

following series:

$$\left.\begin{aligned} u_s(x,z) &= u_0(x,z) + \delta u_1(x,z) + \delta^2 u_2(x,z) + \cdots, \\ w_s(x,z) &= w_0(x,z) + \delta w_1(x,z) + \delta^2 w_2(x,z) + \cdots, \\ p_s(x,z) &= p_0(x,z) + \delta p_1(x,z) + \delta^2 p_2(x,z) + \cdots, \\ h_s(x) &= 1 + \delta h_1(x) + \delta^2 h_2(x) + \cdots. \end{aligned}\right\} \tag{4.9}$$

These expansions are then substituted into the steady-state versions of (2.4)–(2.6) and equating powers of δ results in a closed system of equations at each order. The same is done for the corresponding boundary conditions (2.16) and (2.19).

Although this procedure is similar to that used in deriving the Benney equation discussed in Appendix A, there are some significant differences. For example, the Benney equation represents an unsteady evolution equation for h, which emanates from the kinematic condition, whereas in the above approach the kinematic condition is not used. In fact, in our formulation of the problem the approximate steady-state solution for h_s can be found *a priori* by substituting the expansion for h_s into

$$\frac{5\delta^2 We}{6} h_s^3 h_s''' - \frac{6\delta}{Re} h_s h_s'' + \frac{4\delta}{Re}(h_s')^2 - \left[\frac{5\cot\beta}{2Re} h_s^3 + \frac{5\delta}{2Re}\zeta' - \frac{9}{7}\right] h_s' - \frac{15\delta}{4Re}\zeta'' h_s + \left[\frac{5}{2\delta Re} - \frac{5\cot\beta}{2Re}\zeta' + \frac{5\delta^2 We}{6}\zeta'''\right] h_s^3 = \frac{5}{2\delta Re} + \frac{5\delta}{Re}(\zeta')^2. \tag{4.10}$$

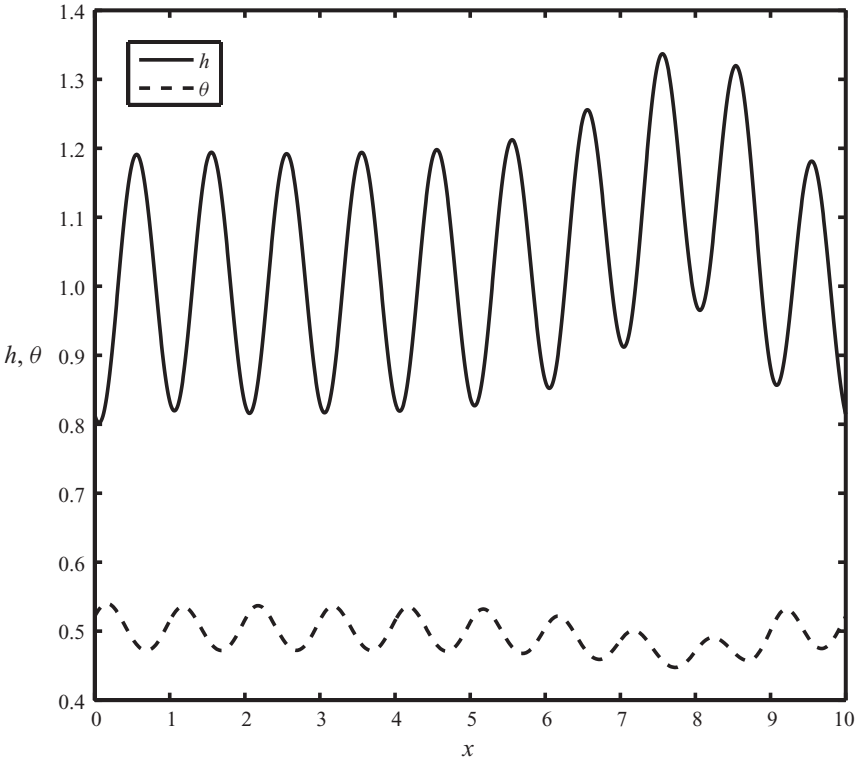

FIGURE 20. Distributions of h and θ at $t = 200$ for the case with $Re = 1$, $\cot\beta = 0.5$, $Bi = 1$, $Ma = 1$, $We = 100$, $a_b = 0.2$, $\delta = 0.1$ and $Pr = 7$ on a computational domain of length $L = 10$.

It is a straightforward exercise to show that if $We = O(1)$, then $h_1(x)$ and $h_2(x)$ are given by

$$\left.\begin{aligned} h_1(x) &= \frac{\cot\beta}{3}\zeta'(x), \\ h_2(x) &= \frac{2}{3}\left(1 + \frac{\cot^2\beta}{3}\right)[\zeta'(x)]^2 + \left(\frac{1}{2} - \frac{2Re\cot\beta}{35} + \frac{\cot^2\beta}{9}\right)\zeta''(x). \end{aligned}\right\} \tag{4.11}$$

Note that for $We = O(1)$ surface-tension effects do not yet enter into the problem. Figure 22 shows a typical comparison between the analytical and numerical solutions for h_s. Provided that the Weber number is of order unity, the agreement is good.

For the case with $We = O(1)$, the leading-order problem arising from (2.4)–(2.6) and (2.16), (2.19) is given by

$$\frac{\partial p_0}{\partial z} = -\frac{3\cot\beta}{Re}, \quad \frac{\partial^2 u_0}{\partial z^2} = -3, \quad \frac{\partial w_0}{\partial z} = -\frac{\partial u_0}{\partial x}, \tag{4.12}$$

subject to the following boundary conditions:

$$\left.\begin{aligned} &u_0 = w_0 = 0 \quad \text{at } z = \zeta(x), \\ &p_0 = \frac{\partial u_0}{\partial z} = 0 \quad \text{at } z = 1 + \zeta(x). \end{aligned}\right\} \tag{4.13}$$

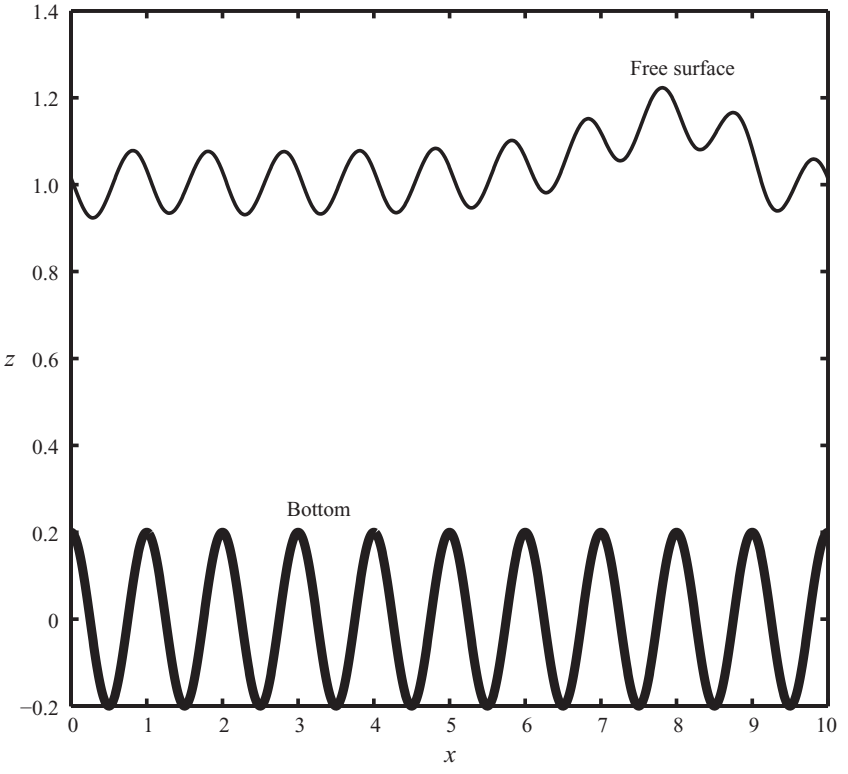

FIGURE 21. Free-surface variations at $t = 200$ for the case with $Re = 1$, $\cot\beta = 0.5$, $Bi = 1$, $Ma = 1$, $We = 100$, $a_b = 0.2$, $\delta = 0.1$ and $Pr = 7$ on a computational domain of length $L = 10$.

The solutions are easily found to be

$$\left.\begin{aligned} p_0(x,z) &= \frac{3\cot\beta}{Re}(1+\zeta-z),\\ u_0(x,z) &= -\tfrac{3}{2}(z-\zeta)^2 + 3(z-\zeta),\\ w_0(x,z) &= -\tfrac{3}{2}\zeta'(z-\zeta)^2 + 3\zeta'(z-\zeta). \end{aligned}\right\} \tag{4.14}$$

We note that although the kinematic condition was not imposed in arriving at the above solutions, $w_0(x,z)$ does, in fact, satisfy the free-surface condition $w_0(x, z=1+\zeta) = u_0(x, z=1+\zeta)\zeta'$. Continuing this procedure and transferring the free-surface condition from $z = h_s(x) + \zeta$ to $z = 1 + \zeta$, we obtain

$$\left.\begin{aligned} u_1(x,z) &= \cot\beta\zeta'\left(\tfrac{3}{2}(z-\zeta)^2 - 2(z-\zeta)\right),\\ u_2(x,z) &= \zeta''\left(\left[\tfrac{1}{2}(z-\zeta)^2 - \tfrac{2}{3}(z-\zeta)\right]\cot^2\beta - (z-\zeta)^3 + 3(z-\zeta)^2 - 3(z-\zeta)\right)\\ &\quad -\zeta'' Re\cot\beta\left(\tfrac{1}{40}(z-\zeta)^6 - \tfrac{3}{20}(z-\zeta)^5 + \tfrac{1}{4}(z-\zeta)^4 - \tfrac{8}{35}(z-\zeta)\right)\\ &\quad +\left(\zeta'\right)^2\left(3(z-\zeta)^2 - 4(z-\zeta) - \tfrac{7}{18}\cot^2\beta(z-\zeta)\right). \end{aligned}\right\} \tag{4.15}$$

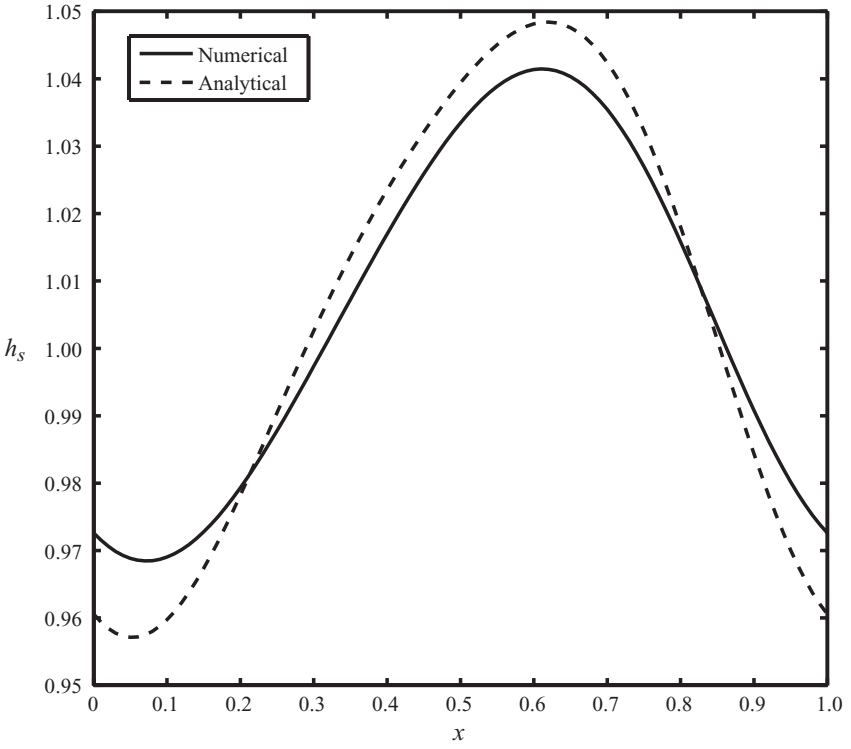

FIGURE 22. Comparison between analytical and numerical solutions for $h_s(x)$ for the isothermal case with $a_b = 0.2$, $\cot\beta = 0.5$, $Re = 1$, $We = 1$ and $\delta = 0.1$.

Equipped with this approximate solution for $u_s(x, z)$, we are now prepared to examine how bottom topography and surface tension affect the stability of the flow. Evaluating u_s on the free surface and averaging over the bottom topography, we obtain

$$\bar{u}_s \approx \tfrac{3}{2} - \left(2 + \tfrac{7}{9}\cot^2\beta\right)\pi^2 a_b^2 \delta^2. \tag{4.16}$$

Defining

$$U_s = \bar{u}_s - \tfrac{3}{2} \approx -\left(2 + \tfrac{7}{9}\cot^2\beta\right)\pi^2 a_b^2 \delta^2 \tag{4.17}$$

as the difference in the mean surface velocity between the uneven and even bottom cases, U_s can be regarded as a mean surface drift resulting from bottom unevenness. This drift is a second-order effect which causes the steady-state flow to slow down slightly, which in turn will have a stabilizing effect. Thus, for negligible surface tension, bottom topography acts to retard the flow. Alternatively, we can interpret this in terms of the steady flow rate, Q_s, where

$$Q_s(x) = \int_{\zeta}^{1+\zeta} u_s(x, z)\,\mathrm{d}z, \tag{4.18}$$

giving an average value of

$$\bar{Q}_s \approx 1 - \left(2 + \tfrac{7}{18}\cot^2\beta\right)\pi^2 a_b^2 \delta^2. \tag{4.19}$$

We see that a consequence of the mean surface drift is a slight reduction in the steady flow rate, and hence mass transport.

For $We = O(1)$, the influence of surface tension enters at higher order. Extending this analysis, we have found that the next non-zero term in the expansion for $\bar{Q}_s$ occurs at order δ^4 and is given by

$$\bar{Q}_s \approx 1 - \left(2 + \tfrac{7}{18}\cot^2\beta\right)\pi^2 a_b^2\delta^2 + f(Re, a_b, \cot\beta)\delta^4 - \tfrac{76}{27}\pi^4 a_b^2 Re\cot\beta We\delta^4, \quad (4.20)$$

where $f(Re, a_b, \cot\beta)$ denotes a complicated function that is independent of We. It is evident that for a fixed bottom configuration $\bar{Q}_s$ decreases with We, which indicates that increasing surface tension stabilizes the flow. Furthermore, the magnitude of the gradient of the variation with We increases with a_b, $\cot\beta$ and δ. These predictions are in agreement with those drawn from the linear stability analysis for $We = O(1)$ as revealed by the results presented in figures 10–13; although the plots are shown for $We \geqslant 10$, the behaviour persists for small We as well. It can be seen in all these figures that the $(Re_{crit}^{even} - Re_{crit})$ curves decrease as We is increased up to the first turning point. As mentioned earlier, a decrease in $(Re_{crit}^{even} - Re_{crit})$ coincides with an increase in Re_{crit}, which signals a stabilizing effect. It is also apparent from figures 10–13 that the rate of increase in Re_{crit} increases with a_b, $\cot\beta$ and δ.

To explain the destabilizing role of bottom topography for large We predicted by the linear stability analysis we proceed as follows. For large Weber numbers and small bottom amplitudes, we expect the free surface to become flattened and located at $z \approx 1$. This assertion is suggested by figure 4 and further supported by figure 23. Also, figure 13 demonstrates that the reversal in stability occurs for small bottom amplitudes as well as for larger bottom amplitudes. Using this and applying the free-surface condition at $z = 1$, the leading-order problem yields

$$u_0(x, z) = -\tfrac{3}{2}(z - \zeta)^2 + 3(1 - \zeta)(z - \zeta). \quad (4.21)$$

The steady and averaged steady flow rates then become

$$Q_s(x) \approx \int_\zeta^1 u_0(x, z)\,\mathrm{d}z = (1 - \zeta)^3 \quad \text{and} \quad \bar{Q}_s \approx 1 + \frac{3}{2}a_b^2, \quad (4.22)$$

respectively. Thus, we see that sufficiently strong surface tension will enhance the averaged steady flow rate and hence destabilize the flow. As a final remark, we point out that since our z-independent model governs q directly, setting the flow rate scale to be the value for steady flow over uneven topography gave us $q_s = 1$. However, the two-dimensional equations analysed above are in terms of the primitive variables, and the flow rate is a derived quantity. Since the velocity has been scaled with that corresponding to flow down an even incline, the obtained flow rate deviates from unity, and reveals the explicit dependence on bottom topography.

5. Concluding remarks

This paper solved the problem of laminar flow down an uneven heated inclined surface. In the absence of buoyancy, thermocapillary effects are responsible for inducing an instability through gradients in the surface tension. This study focused on the interaction between the long-wave thermocapillary instability and the classical long-wave hydrodynamic instability present in isothermal flow. The wavy inclined surface was taken to vary sinusoidally. A mathematical model describing the problem has been derived using the weighted residual technique. In addition, a numerical solution procedure has been proposed and was found to successfully capture the unsteady evolution of the free-surface flow.

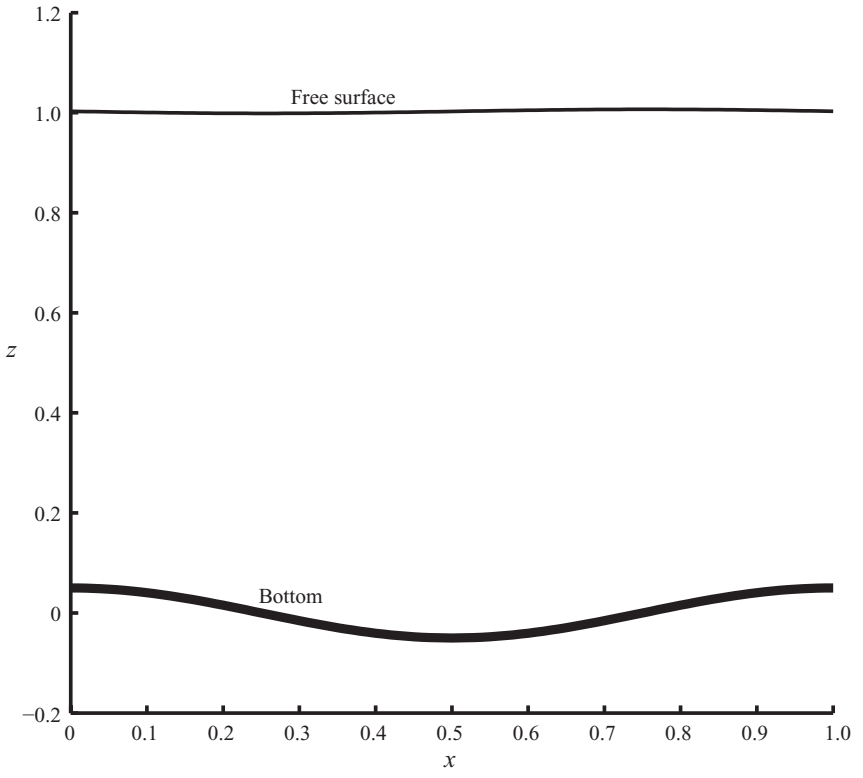

FIGURE 23. Free surface and bottom contour for the case $Re = 0.5$, $\cot\beta = 0.5$, $\delta = 0.1$, $a_b = 0.05$, $We = 10^3$, $Ma = 1$, $Bi = 1$ and $Pr = 7$.

Linear analysis, based on Floquet–Bloch theory, and nonlinear simulations were presented and were found to be in harmony for all cases considered. Some important distinctions in the stability characteristics between an even and a sinusoidally varying bottom were discovered. The key findings from this investigation include the following. The critical Reynolds number for the onset of instability depends on surface tension for an uneven bottom. That is, with or without heating and thermocapillary effects, bottom topography can either stabilize or destabilize the flow depending on surface tension. Heating, on the other hand, has a destabilizing role on the flow for both even and uneven surfaces.

As a means of validating our mathematical formulation, comparisons between numerical simulations and existing experimental data for both even and uneven surfaces have been conducted. Comparisons with direct numerical simulations using the CFX software package have also been carried out. In all cases, the agreement was found to be quite reasonable. A physical explanation as to why bottom topography acting alone stabilizes the flow has been identified; it is the result of an acquired deficit in the averaged steady flow speed (or flow rate) due to bottom unevenness. The intriguing finding that bottom topography can be stabilizing or destabilizing depending on surface tension has been recently reported by D'Alessio *et al.* (2009) and independently by Heining & Aksel (2009) and Häcker & Uecker (2009). All three studies have reached this conclusion using rather different approaches and no explanation was advanced, nor has there been experimental verification of this

behaviour. The approaches adopted by D'Alessio *et al.* (2009) and Häcker & Uecker (2009) were direct ones in that the bottom topography is specified and the stability of the corresponding free surface is investigated. Heining & Aksel (2009), on the other hand, solved the inverse problem by specifying the free surface and then determining the bottom profile responsible for causing that prescribed free surface. The analysis presented in this study can explain the reversal in stability as surface tension is increased. This reversal in stability is the result of a nonlinear interaction between surface tension and bottom topography. For negligible surface tension, a reduced averaged steady flow rate ensues, while for sufficiently strong surface tension an enhanced averaged steady flow rate arises. We have also discovered that in cases where strong surface tension is coupled with bottom unevenness, thermocapillary effects can either stabilize or destabilize the flow depending on the Marangoni number and can also lead to a reversal in stability.

Financial support for this research was provided by the Natural Sciences and Engineering Research Council of Canada. The authors gratefully acknowledge Professor Nuri Aksel for providing us with experimental data.

Appendix A. The first-order Benney equation

An alternate approach in determining the instability threshold is to consider the Benney equation, which is derived here. The Benney equation describes the evolution of the free surface. For our case, we expand u, w, p and T in powers of δ as follows:

$$\left.\begin{aligned} u &= u_0 + \delta u_1 + \cdots, \\ w &= w_0 + \delta w_1 + \cdots, \\ p &= p_0 + \delta p_1 + \cdots, \\ T &= T_0 + \delta T_1 + \cdots. \end{aligned}\right\} \tag{A 1}$$

Substituting these into (2.8)–(2.11) then leads to a hierarchy of problems at various orders. At each order n the quantities u_n, w_n, p_n and T_n can be found by applying the boundary conditions (2.16), (2.19) and (2.20) which are also expanded in powers of δ. Evaluating these expressions at $z = z_1$ and inserting them into the kinematic condition yields to first-order

$$\frac{\partial h}{\partial t} + u_0(z_1)\left(\frac{\partial h}{\partial x} + \zeta'\right) - w_0(z_1) + \delta\left[u_1(z_1)\left(\frac{\partial h}{\partial x} + \zeta'\right) - w_1(z_1)\right] = 0. \tag{A 2}$$

Determining u_n, w_n, p_n, T_n is a straightforward, albeit tedious, task. Since little is gained in the details, we omit the algebra and move directly to the final result for the first-order Benney equation for an uneven bottom:

$$\begin{aligned} \frac{\partial h}{\partial t} + \frac{\partial}{\partial x}(h^3) + \delta\frac{\partial}{\partial x}\Bigg[\frac{6Re}{5}h^6\frac{\partial h}{\partial x} + \frac{ReMaBi}{2}\frac{h^2}{(1+Bih)^2}\frac{\partial h}{\partial x} \\ - \cot\beta h^3\left(\frac{\partial h}{\partial x} + \zeta'\right) + \frac{\delta^2 WeRe}{3}h^3\left(\frac{\partial^3 h}{\partial x^3} + \zeta'''\right)\Bigg] = 0. \end{aligned} \tag{A 3}$$

For the even bottom case having $\zeta = 0$, we linearize (A 3) using $h = 1 + \hat{h}$ and introduce the perturbation $\hat{h} = h_0 e^{ikx} e^{\sigma t}$. It then easily follows that the instability

threshold becomes

$$Re_{crit}^{even} = \frac{10(1+Bi)^2\cot\beta}{5MaBi + 12(1+Bi)^2}, \tag{A 4}$$

which is identical to the result obtained in § 3 given by the expression (3.4).

Appendix B. Coefficients of the linearized perturbation equations

The coefficients appearing in the linearized perturbation equations (3.11) and (3.12) are given by

$$f_1(x) = \frac{34Re + 63\delta h_s'}{14Reh_s} - \frac{19\delta ReMa}{336}h_s\theta_s', \tag{B 1}$$

$$f_2(x) = \frac{70 - 112\delta^2(h_s')^2 + 168\delta^2 h_s h_s'' - 72\delta Reh_s' + 105\delta^2\zeta'' h_s + 70\delta^2\zeta' h_s' + 140\delta^2(\zeta')^2}{28Re\delta {h_s}^2} - \frac{5\delta ReMa}{112}\left(\frac{3}{2}h_s\theta_s'' + h_s'\theta_s'\right), \tag{B 2}$$

$$f_3(x) = \frac{1}{84Re\delta {h_s}^3}\left(-504\delta^2 h_s h_s'' + 210\delta\cot\beta\zeta' {h_s}^3 + 216Re\delta h_s' - 420 - 70\delta^3 WeRe {h_s}^3 h_s''' - 210{h_s}^3 - 840\delta^2(\zeta')^2 + 672\delta^2(h_s')^2 - 420\delta^2 h_s'\zeta' - 70\delta^3 WeRe {h_s}^3\zeta''' - 315\delta^2\zeta'' h_s + 210\delta\cot\beta {h_s}^3 h_s'\right) - \frac{15\delta ReMa}{224}\theta_s'', \tag{B 3}$$

$$f_4(x) = \frac{-112\delta h_s' - 18Re + 35\delta\zeta' + 35\cot\beta {h_s}^3}{14Re {h_s}^2} - \frac{5\delta ReMa}{112}\theta_s', \tag{B 4}$$

$$g_1(x) = \frac{3\delta ReMa}{80}h_s(1-\theta_s) - \frac{\delta}{RePr}, \tag{B 5}$$

$$g_2(x) = \frac{27}{20h_s} - \frac{\delta h_s'}{RePrh_s} - \frac{3\delta ReMa}{40}(2h_s\theta_s' - h_s'[1-\theta_s]), \tag{B 6}$$

$$g_3(x) = \frac{3(1+Bih_s)}{\delta RePrh_s^2} - \frac{3\delta ReMa}{80}(h_s\theta_s'' + 2h_s'\theta_s') - \frac{\delta}{RePr}\left(-\frac{h_s''}{h_s} + \left(2 - \frac{3}{2}Bih_s\right)\left(\frac{h_s'}{h_s}\right)^2 + \frac{3\zeta'(1-Bih_s)h_s'}{h_s^2} - \frac{3\zeta''}{2h_s} - \frac{3Bi(\zeta')^2}{2h_s}\right), \tag{B 7}$$

$$g_4(x) = \frac{27\theta_s'}{20h_s^2} + \frac{3Bi\theta_s}{\delta RePrh_s^2} - \frac{\delta}{RePr}\left([1-\theta_s]\frac{h_s''}{h_s^2} + \frac{2\theta_s''}{h_s} + \frac{h_s'\theta_s'}{h_s^2} - \frac{3}{2}Bi\theta_s\left(\frac{h_s'}{h_s}\right)^2 - \frac{3Bi\zeta' h_s'\theta_s}{h_s^2} + \frac{3\zeta''(1-\theta_s)}{2h_s^2} - \frac{3Bi(\zeta')^2\theta_s}{2h_s^2}\right) - \frac{3\delta ReMa}{80} \times \left(6(\theta_s')^2 - 3[1-\theta_s]\theta_s'' - 4h_s'[1-\theta_s]\frac{\theta_s'}{h_s}\right), \tag{B 8}$$

$$g_5(x) = -\frac{\delta}{RePr}\left(\frac{\theta_s'}{h_s} - \frac{3Bih_s'\theta_s}{h_s} - \frac{4h_s'[1-\theta_s]}{h_s^2} - \frac{3\zeta'[1-(1-Bih_s)\theta_s]}{h_s^2}\right) + \frac{3\delta ReMa}{40}(1-\theta_s)\theta_s'. \tag{B 9}$$

Appendix C. Numerical solution procedure

For numerical purposes, we begin by expressing the governing equations (2.28)–(2.30) in terms of the flow variables h, q and $\phi = h(\theta - 1)$. From the relation $(T-1)h = (\theta-1)(z-\zeta)$ it follows that the variable ϕ is related to T through

$$\int_{\zeta}^{\zeta+h} (T-1)\,\mathrm{d}z = \frac{\phi}{2}, \tag{C 1}$$

and thus, ϕ is proportional to the lineal heat content stored in the fluid layer. The dimensionless equations then become as follows:

$$\frac{\partial h}{\partial t} + \frac{\partial q}{\partial x} = 0, \tag{C 2}$$

$$\begin{aligned}\frac{\partial q}{\partial t} + \frac{\partial}{\partial x}\left[\frac{9}{7}\frac{q^2}{h} + \frac{5\cot\beta}{4Re}h^2 + \frac{5Ma}{4}\frac{\phi}{h}\right] &= \frac{q}{7h}\frac{\partial q}{\partial x} + \frac{5}{2\delta Re}\left(h - \frac{q}{h^2}\right) - \frac{5\cot\beta}{2Re}\zeta' h \\ &+ \frac{5\delta^2 We}{6}h\left(\frac{\partial^3 h}{\partial x^3} + \zeta'''\right) + \frac{\delta ReMa}{48}\left[h\frac{\partial^2\phi}{\partial x\partial t} - \frac{\partial h}{\partial x}\frac{\partial\phi}{\partial t} + \frac{26}{7}\frac{\partial q}{\partial x}\frac{\partial\phi}{\partial x} + \phi\frac{\partial^2 q}{\partial x^2}\right] \\ &+ \frac{\delta ReMa}{112}\left[-10\frac{q}{h}\frac{\partial h}{\partial x}\frac{\partial\phi}{\partial x} + 10\frac{q\phi}{h^2}\left(\frac{\partial h}{\partial x}\right)^2 - 11\frac{\phi}{h}\frac{\partial h}{\partial x}\frac{\partial q}{\partial x} + \frac{15}{2}q\frac{\partial^2\phi}{\partial x^2} - \frac{15}{2}\frac{q\phi}{h}\frac{\partial^2 h}{\partial x^2}\right] \\ &+ \frac{\delta}{Re}\left[\frac{9}{2}\frac{\partial^2 q}{\partial x^2} - \frac{9}{2h}\frac{\partial h}{\partial x}\frac{\partial q}{\partial x} - \frac{6q}{h}\frac{\partial^2 h}{\partial x^2} + \frac{4q}{h^2}\left(\frac{\partial h}{\partial x}\right)^2 - \frac{5\zeta' q}{2h^2}\frac{\partial h}{\partial x} - \frac{15\zeta'' q}{4h} - \frac{5(\zeta')^2 q}{h^2}\right],\end{aligned} \tag{C 3}$$

$$\begin{aligned}\frac{\partial\phi}{\partial t} + \frac{\partial}{\partial x}\left[\frac{27}{20}\frac{q\phi}{h}\right] &= \frac{7\phi}{40h}\frac{\partial q}{\partial x} - \frac{3}{\delta Peh}\left(Bi(h+\phi) + \frac{\phi}{h}\right) + \frac{3\delta ReMa}{80}\left[\phi\frac{\partial^2\phi}{\partial x^2}\right. \\ &\left. + 2\left(\frac{\partial\phi}{\partial x}\right)^2 - \frac{4\phi}{h}\frac{\partial h}{\partial x}\frac{\partial\phi}{\partial x} - \frac{\phi^2}{h}\frac{\partial^2 h}{\partial x^2} + \frac{2\phi^2}{h^2}\left(\frac{\partial h}{\partial x}\right)^2\right] + \frac{\delta}{RePr}\left[\frac{\partial^2\phi}{\partial x^2} - \frac{1}{h}\frac{\partial h}{\partial x}\frac{\partial\phi}{\partial x}\right. \\ &\left. - \frac{2\phi}{h}\frac{\partial^2 h}{\partial x^2} + \frac{3\phi}{h^2}\left(\frac{\partial h}{\partial x}\right)^2 + \frac{3\zeta'\phi}{h^2}\frac{\partial h}{\partial x} - \frac{3\zeta''\phi}{2h} - \frac{3Bi}{2}\left(1 + \frac{\phi}{h}\right)\left(\zeta' + \frac{\partial h}{\partial x}\right)^2\right].\end{aligned} \tag{C 4}$$

For an isothermal fluid, $\phi = Ma = Bi = 0$ and the modified IBL equations for a wavy incline (D'Alessio *et al.* 2009) are recovered, as expected.

To solve the above system numerically, we first express these equations in the form

$$\left.\begin{aligned}\frac{\partial h}{\partial t} + \frac{\partial q}{\partial x} &= 0, \\ \frac{\partial q}{\partial t} + \frac{\partial}{\partial x}\left(\frac{9}{7}\frac{q^2}{h} + \frac{5\cot\beta}{4Re}h^2 + \frac{5Ma}{4}\frac{\phi}{h}\right) &= \psi_1 + \chi_1, \\ \frac{\partial\phi}{\partial t} + \frac{\partial}{\partial x}\left(\frac{27}{20}\frac{q\phi}{h}\right) &= \psi_2 + \chi_2,\end{aligned}\right\} \tag{C 5}$$

where the source terms $\psi_1 = 5(h - q/h^2)/(2\delta Re)$ and $\psi_2 = -3[B(1+\phi/h)+\phi/h^2]/(\delta Pe)$ while χ_1 and χ_2 can be easily determined from (C 3) and (C 4). To solve this system of equations, the fractional-step splitting strategy (LeVeque 2002) was implemented. This technique decouples the advective and diffusive components, that is, we first

solve

$$\left.\begin{aligned} \frac{\partial h}{\partial t}+\frac{\partial q}{\partial x}&=0,\\ \frac{\partial q}{\partial t}+\frac{\partial}{\partial x}\left(\frac{9}{7}\frac{q^2}{h}+\frac{5\cot\beta}{4Re}h^2+\frac{5Ma}{4}\frac{\phi}{h}\right)&=\psi_1(h,q),\\ \frac{\partial \phi}{\partial t}+\frac{\partial}{\partial x}\left(\frac{27}{20}\frac{q\phi}{h}\right)&=\psi_2(h,\phi), \end{aligned}\right\} \tag{C 6}$$

over a time step Δt, and then solve

$$\left.\begin{aligned} \frac{\partial q}{\partial t}&=\chi_1\left(h,q,\phi,\frac{\partial h}{\partial x},\frac{\partial q}{\partial x},\frac{\partial \phi}{\partial x},\frac{\partial \phi}{\partial t},\frac{\partial^2 h}{\partial x^2},\frac{\partial^2 q}{\partial x^2},\frac{\partial^2 \phi}{\partial x^2},\frac{\partial^2 \phi}{\partial x\partial t},\frac{\partial^3 h}{\partial x^3},x\right),\\ \frac{\partial \phi}{\partial t}&=\chi_2\left(h,\phi,\frac{\partial h}{\partial x},\frac{\partial q}{\partial x},\frac{\partial \phi}{\partial x},\frac{\partial^2 h}{\partial x^2},\frac{\partial^2 \phi}{\partial x^2},x\right), \end{aligned}\right\} \tag{C 7}$$

using the solution obtained from the first step as an initial condition for the second step. The second step then returns the solution for q and ϕ at the new time $t+\Delta t$.

The first step involves solving a nonlinear system of hyperbolic conservation laws which, when expressed in vector form, can be written compactly as

$$\left.\begin{aligned} &\frac{\partial \boldsymbol{U}}{\partial t}+\frac{\partial \boldsymbol{F}(\boldsymbol{U})}{\partial x}=\boldsymbol{B}(\boldsymbol{U}),\\ &\text{where } \boldsymbol{U}=\begin{bmatrix} h\\ q\\ \phi \end{bmatrix},\quad \boldsymbol{F}(\boldsymbol{U})=\begin{bmatrix} q\\ \dfrac{9}{7}\dfrac{q^2}{h}+\dfrac{5\cot\beta}{4Re}h^2+\dfrac{5Ma}{4}\dfrac{\phi}{h}\\ \dfrac{27}{20}\dfrac{q\phi}{h} \end{bmatrix},\quad \boldsymbol{B}(\boldsymbol{U})=\begin{bmatrix} 0\\ \psi_1\\ \psi_2 \end{bmatrix}. \end{aligned}\right\} \tag{C 8}$$

While there are several schemes available to solve such a system, because of the complicated eigenstructure of the above system eigen-based methods will not be practical. Instead, MacCormack's method was adopted due to its relative simplicity. This is a conservative second-order accurate finite difference scheme, which correctly captures discontinuities and converges to the physical weak solution of the problem. LeVeque & Yee (1990) extended MacCormack's method to include source terms via the explicit predictor–corrector scheme

$$\left.\begin{aligned} \boldsymbol{U}_j^*&=\boldsymbol{U}_j^n-\frac{\Delta t}{\Delta x}\left[\boldsymbol{F}\left(\boldsymbol{U}_{j+1}^n\right)-\boldsymbol{F}\left(\boldsymbol{U}_j^n\right)\right]+\Delta t\ \boldsymbol{B}\left(\boldsymbol{U}_j^n\right),\\ \boldsymbol{U}_j^{n+1}&=\frac{1}{2}\left(\boldsymbol{U}_j^n+\boldsymbol{U}_j^*\right)-\frac{\Delta t}{2\Delta x}[\boldsymbol{F}(\boldsymbol{U}_j^*)-\boldsymbol{F}(\boldsymbol{U}_{j-1}^*)]+\frac{\Delta t}{2}\boldsymbol{B}(\boldsymbol{U}_j^*), \end{aligned}\right\} \tag{C 9}$$

where the notation $\boldsymbol{U}_j^n\equiv\boldsymbol{U}(x_j,t_n)$ is utilized with Δx denoting the uniform grid spacing and Δt is the time step.

The second step reduces to solving a coupled system of generalized one-dimensional nonlinear diffusion equations having the form

$$\left.\begin{aligned}
\frac{\partial q}{\partial t} &= \delta\left(\frac{9}{2Re}+\frac{ReMa}{48}\phi\right)\frac{\partial^2 q}{\partial x^2}+\left[S_1+\frac{q}{7h}+\frac{\delta ReMa}{16}\left(\frac{26}{21}\frac{\partial\phi}{\partial x}-\frac{11}{7h}\frac{\partial h}{\partial x}\phi\right)\right]\\
&\quad\times\frac{\partial q}{\partial x}+S+\frac{\delta ReMa}{48}\left(h\frac{\partial^2\phi}{\partial x\partial t}-\frac{\partial h}{\partial x}\frac{\partial\phi}{\partial t}\right)+\left[S_0+\frac{\delta ReMa}{112}\left(\frac{10}{h^2}\left(\frac{\partial h}{\partial x}\right)^2\phi\right.\right.\\
&\quad\left.\left.-\frac{10}{h}\frac{\partial h}{\partial x}\frac{\partial\phi}{\partial x}+\frac{15}{2}\frac{\partial^2\phi}{\partial x^2}-\frac{15}{2h}\frac{\partial^2 h}{\partial x^2}\phi\right)\right]q,\\
\frac{\partial\phi}{\partial t} &= \delta\left(\frac{1}{RePr}+\frac{3ReMa}{80}\phi\right)\frac{\partial^2\phi}{\partial x^2}+\frac{3\delta ReMa}{40}\left(\frac{\partial\phi}{\partial x}\right)^2+\hat{S}\\
&\quad+\left(\hat{S}_1-\frac{3\delta ReMa}{20h}\frac{\partial h}{\partial x}\phi\right)\frac{\partial\phi}{\partial x}+\left(\hat{S}_0+\frac{7}{40h}\frac{\partial q}{\partial x}\right)\phi+\hat{S}_2\phi^2,
\end{aligned}\right\}\tag{C 10}$$

where the functions S, S_0, S_1 and $\hat{S}$, $\hat{S}_0$, $\hat{S}_1$, $\hat{S}_2$ are easily obtainable from (C 3) and (C 4). Since h is known from the first step and remains constant during the second step, the functions S, S_0, S_1, $\hat{S}$, $\hat{S}_0$, $\hat{S}_1$, $\hat{S}_2$ are known. Discretizing the above equations using the Crank–Nicolson scheme, imposing periodicity conditions and using the output from the first step as an initial condition, leads to nonlinear systems of algebraic equations which were solved iteratively. A robust algorithm, taking advantage of the structure and sparseness of the resulting linearized systems, was used to speed up the iterative process. It was found that convergence was reached quickly, typically in less than five iterations.

The evolution of the unsteady flow can be computed by imposing perturbed steady-state solutions as initial conditions. The steady-state solutions, given by $q=q_s=1$, $h=h_s(x)$ and $\phi=\phi_s(x)$, were numerically generated by solving

$$\begin{aligned}
&\frac{5\delta^2 We}{6}h_s^3h_s'''-\delta\left(\frac{6}{Re}+\frac{15ReMa}{224}\phi_s\right)h_sh_s''+\delta\left(\frac{4}{Re}+\frac{5ReMa}{56}\phi_s\right)(h_s')^2\\
&\quad-\left[\frac{5\cot\beta}{2Re}h_s^3+\frac{5\delta}{2Re}\zeta'+\frac{5\delta ReMa}{56}h_s\phi_s'-\frac{5Ma}{4}\phi_s-\frac{9}{7}\right]h_s'-\left(\frac{15\delta}{4Re}\zeta''+\frac{5Ma}{4}\phi_s'\right)h_s\\
&\quad+\frac{15\delta ReMa}{224}\phi_s''h_s^2+\left[\frac{5}{2\delta Re}-\frac{5\cot\beta}{2Re}\zeta'+\frac{5\delta^2 We}{6}\zeta'''\right]h_s^3=\frac{5}{2\delta Re}+\frac{5\delta}{Re}(\zeta')^2,
\end{aligned}\tag{C 11}$$

$$\begin{aligned}
&\delta\left(\frac{1}{RePr}+\frac{3ReMa}{80}\phi_s\right)h_s^2\phi_s''+\frac{3\delta ReMa}{40}h_s^2(\phi_s')^2-\left[\frac{3\delta ReMa}{20}h_s'\phi_s+\frac{\delta}{RePr}h_s'\right.\\
&\quad\left.+\frac{27}{20}\right]h_s\phi_s'+\left[\frac{27}{20}h_s'-\frac{3}{\delta RePr}(1+Bih_s)+\frac{3\delta}{RePr}(\zeta'+h_s')h_s'-\frac{\delta}{RePr}\right.\\
&\quad\left.\times\left(\frac{3}{2}\zeta''+2h_s''\right)h_s-\frac{3Bi\delta}{2RePr}h_s(\zeta'+h_s')^2\right]\phi_s+\frac{3\delta ReMa}{80}[2(h_s')^2-h_sh_s'']\phi_s^2\\
&\quad=\frac{3Bi}{\delta RePr}h_s^2+\frac{3Bi\delta}{2RePr}h_s^2(\zeta'+h_s')^2,
\end{aligned}\tag{C 12}$$

with the prime denoting differentiation with respect to x. For the special case of an even bottom (i.e. $\zeta = 0$) the following solutions emerge:

$$h_s = 1 \quad \text{and} \quad \phi_s = -\frac{Bi}{1+Bi}, \tag{C 13}$$

from which it immediately follows that

$$\theta_s = \frac{1}{1+Bi} \quad \text{and} \quad T_s(z) = 1 - \frac{Biz}{1+Bi}. \tag{C 14}$$

The MATLAB routine bvp4c was implemented to integrate the coupled system of differential equations (C 11) and (C 12).

REFERENCES

Alekseenko, S., Nakoryakov, V. & Pokusaev, B. 1985 Wave formation on a vertical falling liquid film. *AIChE J.* **31**, 1446–1460.

Balmforth, N. J. & Mandre, S. 2004 Dynamics of roll waves. *J. Fluid Mech.* **514**, 1–33.

Bénard, H. 1900 Les tourbillons cellulaires dans une mappe liquide. *Rev. Gen. Sci. Pures et Appl.* **11**, 1261–1271.

Benjamin, T. B. 1957 Wave formation in laminar flow down an inclined plane. *J. Fluid Mech.* **2**, 554–574.

Benney, D. J. 1966 Long waves on liquid films. *J. Math. Phys.* **45**, 150–155.

Brock, R. R. 1969 Development of roll-wave trains in open channels. *J. Hydraul. Div.* **95** (HY4), 1401–1427.

Brook, B. S., Pedley, T. J. & Falle, S. A. 1999 Numerical solutions for unsteady gravity-driven flows in collapsible tubes: evolution and roll-wave instability of a steady state. *J. Fluid Mech.* **396**, 223–256.

Chang, H.-C. 1994 Wave evolution on a falling film. *Annu. Rev. Fluid Mech.* **26**, 103–136.

Chang, H.-C., Demekhin, E. A. & Kalaidin, E. 2000 Coherent structures, self-similarity and universal roll wave coarsening dynamics. *Phys. Fluids* **12**, 2268–2278.

Craster, R. V. & Matar, O. K. 2009 Dynamics and stability of thin liquid films. *Rev. Mod. Phys.* **81**, 1131–1198.

D'Alessio, S. J. D., Pascal, J. P. & Jasmine, H. A. 2009 Instability in gravity-driven flow over uneven surfaces. *Phys. Fluids* **21**, 062105.

Davalos-Orozco, L. A. 2007 Nonlinear instability of a thin film flowing down a smoothly deformed surface. *Phys. Fluids* **19**, 074103.

Davalos-Orozco, L. A. 2008 Instabilities of thin films flowing down flat and smoothly deformed walls. *Microgravity Sci. Technol.* **20**, 225–229.

Goussis, D. A. & Kelly, R. E. 1991 Surface wave and thermocapillary instabilities in a liquid film flow. *J. Fluid Mech.* **223**, 25–45 and erratum *J. Fluid Mech.* **226**, 663.

Häcker, T. & Uecker, H. 2009 An integral boundary layer equation for film flow over inclined wavy bottoms. *Phys. Fluids* **21**, 092105.

Heining, C. & Aksel, N. 2009 Bottom reconstruction in thin-film flow over topography: steady solution and linear stability. *Phys. Fluids* **21**, 083605.

Heining, C., Bontozoglou, V., Aksel, N. & Wierschem, A. 2009 Nonlinear resonance in viscous films on inclined wavy planes. *Intl J. Multiphase Flow* **35**, 78–90.

Joo, S. W., Davis, S. H. & Bankoff, S. G. 1991 Long-wave instabilities of heated falling films: two dimensional theories of uniform layers. *J. Fluid Mech.* **230**, 117–146.

Julien, P. & Hartley, D. 1986 Formation of roll waves in laminar sheet flow. *J. Hydraul. Res.* **24**, 5–17.

Kalliadasis, S., Demekhin, E. A., Ruyer-Quil, C. & Velarde, M. G. 2003*a* Thermocapillary instability and wave formation on a film falling down a uniformly heated plane. *J. Fluid Mech.* **492**, 303–338.

Kalliadasis, S., Kiyashko, A. & Demekhin, E. A. 2003*b* Marangoni instability of a thin liquid film heated from below by a local heat source. *J. Fluid Mech.* **475**, 377–408.

Kapitza, P. L. & Kapitza, S. P. 1949 Wave flow of thin layers of a viscous fluid. Part III. Experimental study of undulatory flow conditions. *Soc. Phys. J. Exp. Theor. Phys.* **19**, 105–120.

Khayat, R. E. & Kim, K. T. 2006 Thin-film flow of a viscoelastic fluid on an axisymmetric substrate of arbitrary shape. *J. Fluid Mech.* **552**, 37–71.

Kranenburg, C. 1992 On the evolution of roll waves. *J. Fluid Mech.* **245**, 249–261.

LeVeque, R. J. 2002 *Finite Volume Methods for Hyperbolic Problems*. Cambridge University Press.

LeVeque, R. J. & Yee, H. C. 1990 A study of numerical methods for hyperbolic conservation laws with stiff source terms. *J. Comput. Phys.* **86**, 187–210.

Lin, S. P. 1974 Finite amplitude side-band stability of viscous film. *J. Fluid Mech.* **63**, 417–429.

Lin, S. P. 1975 Stability of a liquid film down a heated inclined plane. *Lett. Heat Mass Transfer* **2**, 361–370.

Liu, J., Paul, J. D. & Gollub, J. P. 1993 Measurements of the primary instabilities of film flows. *J. Fluid Mech.* **250**, 69–101.

Liu, J., Schneider, B. & Gollub, J. P. 1995 Three-dimensional instabilities of film flows. *Phys. Fluids* **7**, 55–67.

Mukhopadhyay, A. & Mukhopadhyay, A. 2007 Nonlinear stability of viscous film flowing down an inclined plane with linear temperature variation. *J. Phys.* D: *Appl. Phys.* **40**, 5683–5690.

Nepomnyashchy, A. A. 1974 Stability of wave regimes in a film flowing down an inclined plane. *Izv. Akad. Nauk SSSR Mekh. Zhidk. Gaza* **3**, 28–34.

Nepomnyashchy, A. A., Velarde, M. G. & Colinet, P. 2002 *Interfacial Phenomena and Convection*. CRC.

Oron, A., Davis, S. H. & Bankoff, S. G. 1997 Long-scale evolution of thin liquid films. *Rev. Mod. Phys.* **69**, 931–980.

Oron, A. & Gottlieb, O. 2004 Subcritical and supercritical bifurcations of the first and second order Benney equations. *J. Engng Math.* **50**, 121–140.

Oron, A. & Heining, C. 2008 Weighted-residual integral boundary-layer model for the nonlinear dynamics of thin liquid films falling on an undulating vertical wall. *Phys. Fluids* **20**, 082102.

Pearson, J. 1958 On convection cells induced by surface tension. *J. Fluid Mech.* **4**, 489–500.

Prokopiou, T., Cheng, M. & Chang, H.-C. 1991 Long waves on inclined films at high Reynolds number. *J. Fluid Mech.* **222**, 665–691.

Ramaswamy, B., Chippada, S. & Joo, S. W. 1996 A full-scale numerical study of interfacial instabilities in thin-film flows. *J. Fluid Mech.* **325**, 163–194.

Rosenau, P., Oron, A. & Hyman, J. 1992 Bounded and unbounded patterns of the Benney equation. *Phys. Fluids* A **4**, 1102–1104.

Ruyer-Quil, C. & Manneville, P. 2000 Improved modeling of flows down inclined planes. *Eur. Phys. J.* B **15**, 357–369.

Ruyer-Quil, C. & Manneville, P. 2002 Further accuracy and convergence results on the modeling of flows down inclined planes by weighted-residual approximations. *Phys. Fluids* **14**, 170–183.

Ruyer-Quil, C., Scheid, B., Kalliadasis, S., Velarde, M. G. & Zeytounian, R. Kh. 2005 Thermocapillary long waves in a liquid film flow. Part 1. Low-dimensional formulation. *J. Fluid Mech.* **538**, 199–222.

Salamon, T. R., Armstrong, R. C. & Brown, R. A. 1994 Traveling waves on vertical films: Numerical analysis using the finite element method. *Phys. Fluids* **6**, 2202–2220.

Samanta, A. 2008 Stability of liquid film falling down a vertical non-uniformly heated wall. *Physica* D **237**, 2587–2598.

Scheid, B., Ruyer-Quil, C., Kalliadasis, S., Velarde, M. G. & Zeytounian, R. Kh. 2005*a* Thermocapillary long waves in a liquid film flow. Part 2. Linear stability and nonlinear waves. *J. Fluid Mech.* **538**, 223–244.

Scheid, B., Ruyer-Quil, C., Thiele, U., Kabov, O. A., Legros, J. C. & Colinet, P. 2005*b* Validity domain of the Benney equation including the Marangoni effect for closed and open flows. *J. Fluid Mech.* **527**, 303–335.

Scheid, B., Ruyer-Quil, C. & Manneville, P. 2006 Wave patterns in film flows: modelling and three-dimensional waves. *J. Fluid Mech.* **562**, 183–222.

Scriven, L. & Sternling, C. 1964 On cellular convection driven by surface-tension gradients: effects of mean surface tension and surface viscosity. *J. Fluid Mech.* **19**, 321–340.

Shkadov, V. Y. 1967 Wave conditions in flow of thin layer of a viscous liquid under the action of gravity. *Izv. Akad. Nauk SSSR Mekh. Zhidk. Gaza* **1**, 43–50.

Smith, K. A. 1966 On convective instability induced by surface-tension gradients. *J. Fluid Mech.* **24**, 401–414.

Smith, M. K. 1990 The mechanism for the long-wave instability in thin liquid films. *J. Fluid Mech.* **217**, 469–485.

Thiele, U., Goyeau, B. & Velarde, M. G. 2009 Stability analysis of thin flow along a heated porous wall. *Phys. Fluids* **21**, 014103.

Tougou, H. 1978 Long waves on a film flow of a viscous fluid down an inclined uneven wall. *J. Phys. Soc. Japan* **44**, 1014–1019.

Trevelyan, P. M. J., Scheid, B., Ruyer-Quil, C. & Kalliadasis, S. 2007 Heated falling films. *J. Fluid Mech.* **592**, 295–334.

Trifonov, Y. Y. 1998 Viscous liquid film flows over a periodic surface. *Intl J. Multiphase Flow* **24**, 1139–1161.

Trifonov, Y. Y. 2007*a* Stability and nonlinear wavy regimes in downward film flows on a corrugated surface. *J. Appl. Mech. Tech. Phys.* **48**, 91–100.

Trifonov, Y. Y. 2007*b* Stability of a viscous liquid film flowing down a periodic surface. *Intl J. Multiph. Flow* **33**, 1186–1204.

Usha, R. & Uma, B. 2004 Long waves on a viscoelastic film flow down a wavy incline. *Intl J. Non-Linear Mech.* **39**, 1589–1602.

Vlachogiannis, M. & Bontozoglou, V. 2002 Experiments on laminar film flow along a periodic wall. *J. Fluid Mech.* **457**, 133–156.

Wierschem, A. & Aksel, N. 2003 Instability of a liquid film flowing down an inclined wavy plane. *Physica* D **186**, 221–237.

Wierschem, A., Lepski, C. & Aksel, N. 2005 Effect of long undulated bottoms on thin gravity-driven films. *Acta Mechanica* **179**, 41–66.

Yih, C.-S. 1963 Stability of liquid flow down an inclined plane. *Phys. Fluids* **6**, 321–334.

Zanuttigh, B. & Lamberti, A. 2002 Roll waves simulation using shallow water equations and weighted average flux method. *J. Hydraul. Res.* **553**, 610–622.